Journal of Alloys and Compounds 1010 (2025) 177520

Contents lists available at ScienceDirect

Journal of Alloys and Compounds

journal homepage: www.elsevier.com/locate/jalcom

The origin and control of interstitial impurities in refractory complex concentrated alloys

Calvin H. Belcher [a,*], Daisy Kamp [a], Sydney To [a], Yemao Lu [b], Delphine Chassaing [b], Torben Boll [b], Benjamin E. MacDonald [a], Elizabeth M.Y. Lee [a,d], Diran Apelian [a], Enrique J. Lavernia [a,c]

[a] Department of Materials Science and Engineering, University of California, Irvine, Irvine, CA 92617, USA
[b] Karlsruhe Nano Micro Facilities, Karlsruhe Institute for Technology, Karlsruhe 76131, Germany
[c] Department of Materials Science and Engineering, J. Mike Walker '66 Department of Mechanical Engineering, Texas A&M University, College Station, TX 77843, USA
[d] Department of Chemical and Biomolecular Engineering, University of California, Irvine, Irvine, CA 92617, USA

ARTICLE INFO

Keywords:
Refractory complex concentrated alloys
Plasma arc melting
Atom probe tomography
Density functional theory
Embrittlement
Interstitial impurities
Grain Boundaries

ABSTRACT

Interstitial impurities, primarily O and N, inadvertently introduced during the processing of refractory complex concentrated alloys (RCCAs) significantly limit the mechanical properties of the alloys at room temperature. Plasma arc melting (PAM) has facilitated the quest for RCCAs, showcasing remarkable combinations of strength and ductility. In this work, the composition and chemistry of residual gases in the PAM chamber environment during arc melting and the interstitial impurities in elemental feedstocks were analyzed to quantify the origin of O and N during synthesis. Moreover, the thermodynamic mechanisms governing the origin of interstitial impurities in arc-melted MoNbTaW RCCAs were discussed. With an understanding of the mechanisms governing the content of interstitial impurities in RCCAs during PAM, arc-melted MoNbTaW RCCAs with fewer than 100 ppm O were synthesized. The arc-melted MoNbTaW RCCAs were then characterized using electron microscopy and atom probe tomography to establish the compositional architecture of grain boundaries and thereby elucidate the thermodynamic drive for segregation and oxide formation in MoNbTaW. Additionally, density functional theory calculations of a MoNbTaW grain boundary were employed to analyze the effect of local chemical fluctuations on the O segregation and oxide formation at the grain boundary. This detailed understanding of the thermodynamic mechanisms governing the origin of interstitial impurities and their grain boundary segregation in MoNbTaW RCCAs provides greater context surrounding O interactions in RCCAs, which is key for the successful development of refractory alloys with unique combinations of strength and ductility.

1. Introduction

Refractory complex concentrated alloys (RCCAs), also known as refractory high entropy alloys, are body-centered cubic (BCC) non-dilute alloys made up of 3 or more constituent elements in near equiatomic composition using transition metals from subgroups IV, V, and VI. Their discovery has led to a resurgence in refractory alloy development to replace superalloys for nuclear, hypersonic, and space applications [1–3]. Thus far, RCCAs show promising mechanical behavior for high-temperature structural applications. However, a major challenge to their development and practical use is their extremely low ductility at room temperature and a lack of design criteria for ductile RCCAs. Many RCCA compositions have been explored in the search for an alloy with both high strength at elevated temperatures and ductility at room temperature [4–8]. In the literature, RCCAs have been studied broadly through two model systems, MoNbTaW and HfNbTaTiZr, due to their significant differences in room temperature ductility which have been attributed to the constituent elements and their modifications to dislocation motion and their sensitivity to interstitial impurities such as O, N, and C [9–11]. The HfNbTaTiZr alloy system has high room-temperature ductility and relatively low sensitivity to interstitial impurities [11,12]. In fact, additions of up to 2 at% O and N could increase the strength and ductility of HfNbTaTiZr systems by forming ordered interstitial complexes [12–16]. The addition of O to systems based on the model HfNbTaTiZr could even result in increased wear resistance [17–19]. On the other hand, the MoNbTaW system is highly sensitive to interstitial

* Corresponding author.
E-mail address: cbelcher@uci.edu (C.H. Belcher).

https://doi.org/10.1016/j.jallcom.2024.177520
Received 12 September 2024; Received in revised form 5 November 2024; Accepted 11 November 2024
Available online 12 November 2024

impurities O, N, and C. In the MoNbTaW system, O, N, and C have a strong tendency to segregate to grain boundaries (GBs) and form intermetallic structures, embrittling the alloy [20–22]. However, additions of B to the MoNbTaW RCCA competed with trace contents of O and N (~100 s ppm) and segregated to GBs [22]. The B, segregated to GBs, improved the GBs' cohesion and the alloy's overall ductility [22]. These recent shifts in RCCA development have underscored the need to understand how interstitial impurities influence the mechanical behavior of the alloys as well as a need for criteria to control interstitial impurities in the alloys. Thus far, a synthesis technique known as plasma arc melting (PAM) has enabled the development and analysis of RCCAs.

PAM is a non-consumable electrode arc melting process that has enabled the development of RCCAs in laboratory-scale settings. During PAM, feedstock elements are placed in a water-cooled Cu crucible in an inert environment, usually Ar, and melted using a high-temperature electric arc, capable of reaching above 3000 °C [23]. Thus far, PAM processes are typically manually operated, not automated. They can result in broad ranges in interstitial impurities in the synthesized RCCAs. By contrast, conventional refractory alloys are processed via vacuum arc remelting (VAR). This industrial, automated processing technique melts alloys from a consumable electrode under an ultra-high vacuum environment and is typically too large for laboratory-scale alloy development. The automated VAR process maintains the arc stability under a high vacuum. The vacuum environment degasses interstitial impurities such as O, N, C, and H from the molten refractory alloys [23,24]. Because VAR techniques achieve such extremely high temperatures in vacuum environments, the vaporization of oxides and degassing of interstitial impurities occurs [25,26]. In PAM techniques, however, where an inert environment is utilized, residual gases can be absorbed into the RCCAs during synthesis. It is important to distinguish PAM and VAR because the near atmospheric pressure in PAM may cause the absorption of interstitial impurities into the molten RCCAs while during VAR, the ultra-high vacuum can remove interstitial impurities from molten alloys [23,24]. The absorption of interstitial impurities into pure metals at moderate temperatures is well understood [27–29]. However, RCCAs studied to date have been synthesized using various techniques, resulting in various RCCAs with broad ranges in interstitial impurity contents. The interstitial impurities in RCCAs from various synthesis techniques are summarized below in Table 1, reprinted from Belcher et al. [30].

Due to the differences in synthesis techniques and unknown absorption thermodynamics of many RCCAs, especially when compared to industrially produced conventional refractory alloys, broad ranges in the contents of O, N, C, and H have been observed in RCCAs. These broad ranges in interstitial impurities may convolute the understanding of the mechanical behavior of RCCAs and thus their development due to varying sensitivities to the interstitial impurities [31]. Thus, there is a need for better control of interstitial impurities to improve the design and synthesis of RCCAs.

Both processing and alloy composition can drive and modify thermodynamic interactions, which can dictate the influence of interstitial impurities in the behavior of RCCAs. While some work has been done to control interstitial impurities in RCCAs, attempting to prevent GB embrittlement, more in-depth thermodynamic understanding is necessary to improve the development and synthesis of RCCAs. In pure metals and dilute alloys, the mechanisms controlling the absorption of interstitial impurities are well understood and modeled. In general, the thermodynamic drive for absorption can be idealized by the Ellingham Diagrams for oxide formation, where the partial pressure of O_2 contributes a thermodynamic drive for the absorption of O atoms into a metal driven by oxide formation enthalpies [25,26]. At a finer scale, for absorption to occur, first the gases being absorbed, such as O_2 or N_2, must dissociate into single atoms near the surface of the metal [32,33]. The dissociated atoms must then adsorb to the surface of the metal, transport across the metal surface, and then finally diffuse throughout the metal [32,33]. Generally, the adsorption of the dissociated atoms is the rate-limiting step in the absorption process, especially if there are several adsorbing species that may compete for adsorption sites on the surface of the metal [33]. By understanding the mechanisms of absorption, models have been developed for pure metals to predict the thermodynamic equilibrium content of O or N in the metals at specified temperatures and partial pressures of O_2 and N_2, respectively. For example, in Nb the thermodynamic equilibrium models for O and N in Nb from G. Horz and Fromm et al. are shown as Eqs. (1) and (2) below [27–29].

$$\log c_O = \frac{1}{2}\log p_{O_2} - 4.5 + \frac{20200}{T} \quad (1)$$

$$\log c_N = \frac{1}{2}\log p_{N_2} - 3.1 + \frac{9300}{T} \quad (2)$$

Where c_O and c_N are the equilibrium content of O and N in Nb, in at%, respectively. The equilibrium content is predicted at specified temperatures, T in K, and partial pressures, p_{O_2} and p_{N_2}, of O_2 and N_2 in Torr in the environment around the metal. The thermodynamic states of pure metals at elevated temperatures and in the presence of O_2 or N_2 may drive absorption and are dictated by the temperatures and starting interstitial impurity contents. Still, they are unknown for non-dilute alloys, such as RCCAs. Once absorbed into a metal, the thermodynamic interactions between the metal elements and interstitial O or N may drive the formation of microstructural features that influence the resultant mechanical properties. For example, in Mo and W, which are sensitive to interstitial impurities above ~100 ppm, O or N interstitial elements can segregate to GBs, embrittling the metals [34,35]. Other metals, such as Nb and V, have higher solubilities of O and N and can remain ductile with up to 1 at% O or N in solution before causing embrittlement [36,37]. However, the competition or synergy of these mechanisms is not well understood in non-dilute alloys such as RCCAs and is necessary for the development and synthesis of high-strength, ductile refractory alloys.

Motivated by the lack of information surrounding the precise origin of interstitial impurities from residual gases during PAM and the mechanisms that govern detrimental segregation to GBs in the MoNbTaW RCCA, the goal of this work is to establish a fundamental understanding of the thermodynamic factors governing the sources and segregation of interstitial impurities in MoNbTaW to progress the development and deployment of RCCAs as engineering materials. Using O and N as the model interstitial impurities, experimental synthesis of the MoNbTaW RCCA through PAM is characterized to provide in-depth thermodynamic understanding of interstitial impurities in RCCAs. For comparison, O and N interstitial impurities in NbTiZr RCCAs were also characterized during experimental PAM synthesis. MoNbTaW RCCAs with relatively high purity, less than 100 ppm O, were achieved in this study. Despite the low contents of O achieved in these alloys, significant GB segregation of O was observed. A detailed characterization of the resulting microstructural features in the synthesized high purity

Table 1
A summary of the techniques used to synthesize conventional refractory alloys and RCCAs, along with the expected range of interstitial impurity content in the alloys from the process, reprinted from Belcher et al. [30].

Technique	Type of Process	Range of interstitial impurities [ppm]
Vacuum Arc Remelting	Vacuum melting and solidification	10–100
Plasma Arc Melting	Inert environment melting and solidification	100–10,000
Magnetron Sputtering	Inert environment solid-state thin film deposition	100–1000
Mechanical Alloying & Sintering	Solid-state severe plastic deformation & powder consolidation	10,000+

MoNbTaW RCCAs was also conducted to observe the nature of interstitial partitioning within the material. This study provides greater thermodynamic understanding of the interactions between interstitial impurities and the constituent metal elements in RCCAs to guide future synthesis and development of refractory alloys.

2. Experimental methods

2.1. MoNbTaW RCCA preparation and analysis

Ingots of equiatomic MoNbTaW RCCAs, 30 g each, were synthesized via PAM in an Arc200 arc melter from Arcast, Inc. (Oxford, Maine, USA). Both commercial and high-purity feedstocks were separately utilized to synthesize the RCCAs. The commercial purity feedstocks were individual elements, 99.95+ % pure by metals basis, and the high purity feedstocks were binary Nb-Ta and Mo-W master alloys with less than 100 ppm O. The measured contents of O, N, C, and H in the various feedstocks are depicted in Fig. 1a below.

The feedstocks were melted into a homogenous alloy and then flipped and remelted 5 times without breaking the chamber's seal in varied PAM environments. Each alloy was molten for a total of ~15 minutes after completing all the flips and remelts. The environments of the PAM chamber were varied using a rotary (rough vacuum ~E-02 Torr) and turbomolecular (high vacuum ~E-05 Torr) pump as well as commercial purity (99.995 %) Ar, research grade purity (99.9999 %) Ar, and Ar – 5 % H_2 forming gas as the backfill gases. Utilizing the vacuum pumps, backfill gases, and chamber purging techniques, 7 distinct environments were prepared in the PAM chamber for RCCA synthesis. For clarity, a key for the nomenclature of the PAM environments and the chamber preparation steps are described below in Table 2.

In each environment, 3 ingots of the equiatomic MoNbTaW RCCA were synthesized to minimize statistical variation in the as-cast RCCAs. Before synthesizing each alloy, residual gases were measured for analysis. The residual gas analysis (RGA) of the PAM chamber was conducted using an RGA 300 quadrupole mass spectrometer from Stanford Research Systems (Sunnyvale, CA, USA) inside a secondary, ultra-high

Table 2
A key for the nomenclature and preparation steps in the PAM chamber to produce the environments investigated in the synthesis of MoNbTaW RCCAs.

PAM Environment Nomenclature	Preparation Steps in the PAM Chamber
R49	Rough vacuum, then backfilled with 99.995 % Ar
RC49	Rough vacuum cycled 3 times, then backfilled with 99.995 % Ar
T49	Rough vacuum cycled 3 times, followed by high vacuum, then backfilled with 99.995 % Ar
T69	Rough vacuum cycled 3 times, followed by high vacuum, then backfilled with 99.9999 % Ar
T69Ti	Rough vacuum cycled 3 times, followed by high vacuum, backfilled with 99.9999 % Ar, then a 5 g Ti Getter was melted for 2 minutes
T49Ti	Rough vacuum cycled 3 times, followed by high vacuum, backfilled with 99.995 % Ar, then a 5 g Ti Getter was melted for 2 minutes
RC5H	Rough vacuum pump cycled 3 times, then backfilled with Ar – 5 % H_2 forming gas

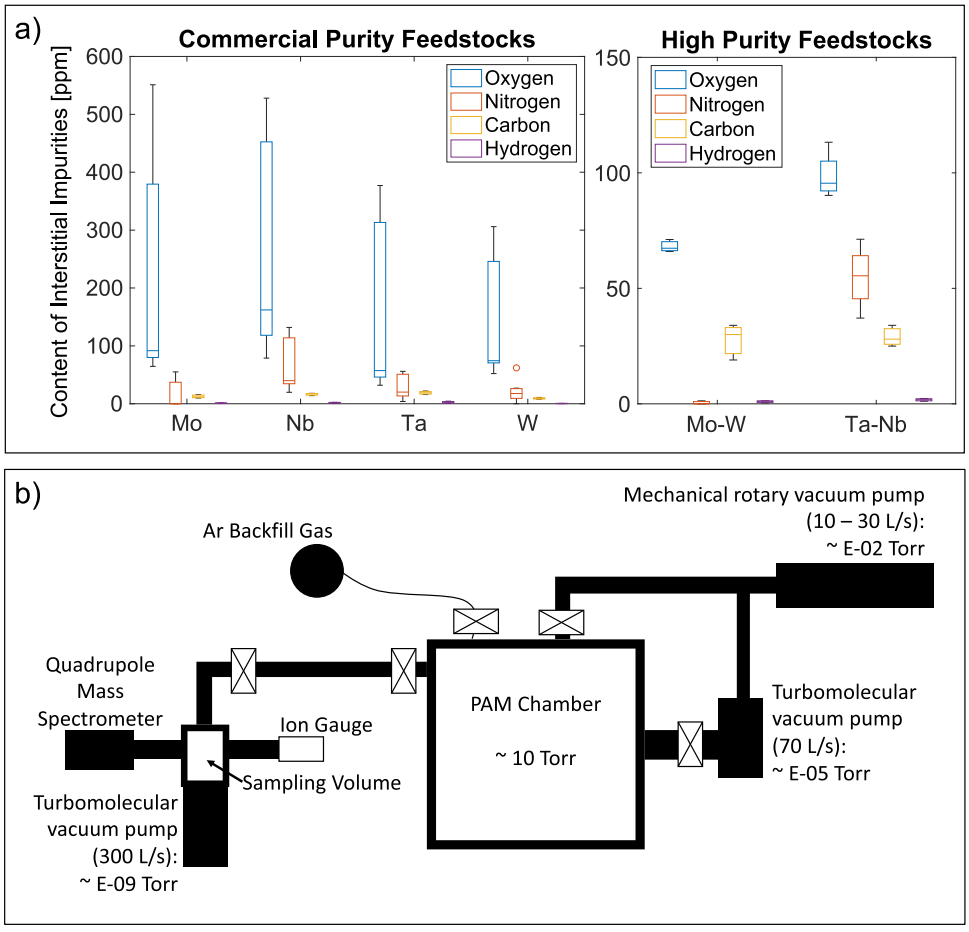

Fig. 1. (a) Grouped bar plots of the contents of O, N, C, and H interstitial impurities in ppm (by weight) in the commercial and high purity feedstocks utilized for RCCA synthesis and (b) a schematic diagram of the PAM chamber and its vacuum systems as well as the vacuum systems of the quadrupole mass spectrometer, utilized to measure the residual gases in the PAM.

vacuum chamber with an ultimate vacuum of ~E-09 Torr. A schematic diagram of the vacuum systems and PAM chamber is provided in Fig. 1b for reference. During RGA, a sampling pressure of 2.0 E-06 Torr was maintained in the sampling volume. The mass spectrometer was run from 1 to 64 at. mass units, and a Faraday Cup detector was used to collect and analyze the ions accelerated by the quadrupole. The mass spectrometer measured the partial pressures of the residual gases in the sampling volume, which was then used to determine the fraction of residual gases in the PAM chamber and, thus, the partial pressures of residual gases in the PAM chamber. The RGA measurements of the PAM chamber are comparable against each other since they are measured using the same dead volume, vacuum chambers, and sampling pressures. Immediately after each RGA measurement of the PAM chamber environment, an RCCA was synthesized in the PAM chamber, and the content of interstitial impurities in the as-cast RCCAs was then measured.

Analysis and discussion of the absorption of interstitial impurities into the RCCAs during PAM synthesis were conducted using thermodynamic equilibrium models for pure Nb. Eqs. (1) and (2) from Grabke et al., Fromm et al., and Fromm were utilized to approximate the equilibrium content of O and N in the MoNbTaW RCCAs [27–29]. This model is used since there is no existing model for non-dilute alloy solutions. There is also no equilibrium O content model developed for Mo or W since there is no equilibrium content of O in Mo or W. It is important to note that the equilibrium models are developed for pure Nb, not non-dilute alloys, so the exact contents of O and N are not expected to be precise, but similar trends in equilibrium contents with partial pressures and temperatures are expected. Furthermore, these equilibrium models are independent of each other, developed for pure gas systems and do not account for any interactions between residual gases which may occur. In the MoNbTaW RCCA, the constituent Mo and W elements have no equilibrium content of O and N, so these elements may result in lower predicted equilibrium contents of O and N [27–29]. The temperatures achieved during PAM were approximated using the Stefan-Boltzmann law and Ohm's law in Eqs. (3) and (4), respectively.

$$\frac{P}{A} = \sigma * T^4 \tag{3}$$

$$P = I * V \tag{4}$$

Where in Eq. (3), P is the power in the form of radiation to the molten alloy, assuming no losses in power to the water-cooled crucible, A is the surface area of the molten alloy, σ is the Boltzmann's constant, and T is the approximated temperature of the molten alloy. In Eq. (3), P is the total power applied to the molten alloy during PAM synthesis and is dependent on the I, current, and V, voltage applied by the arc melter. By assuming there is no power losses to the system, Eqs. (3) and (4) are used to approximate the temperature of the molten alloy, in Eq. (5) below.

$$\sqrt[4]{\frac{I * V}{A * \sigma}} = T \tag{5}$$

The rough approximation of temperature is calculated by assuming all electrical power provided by the power supply goes directly to the molten alloy and there are little to no power losses, which are reasonable assumptions, without detailed understanding of the ionizing gas composition, changing arc gap, and alloy composition. This rough approximation is only meant to provide a general temperature range the alloys were melted at during PAM. It should be noted that the temperatures calculated using Eq. (5) should be considered as approximate ranges rather than precise temperatures. This approximated temperature is used to calculate the predicted equilibrium content of O and N in the alloys using the equilibrium model for pure Nb. Due to the thermal gradients in the molten RCCAs caused by the water-cooled Cu crucible, and power losses that will arise from the electrical resistivity of the components between the power supply and W electrode, this approximation is likely an over estimation of the temperature of the molten RCCAs, but is still a useful approximation since the temperature during PAM could not be directly measured.

2.2. Interstitial impurity content measurement and analysis

Bulk contents of interstitial impurities in the feedstocks and the as-cast RCCAs were measured using inert gas fusion (IGF) and combustion analysis (CA). IGF was conducted using an Eltra Scientific Elementrac ONH-p2 with a maximum operating power of 6000 W to measure O, N, and H and CA was conducted using an Eltra Scientific Elementrac CS-i to measure C. The samples were polished with 600 grit SiC paper and then sectioned into pieces ~ 0.1000 g for ONH analysis and ~ 0.5000 g for C analysis using clean bolt cutters. Ni fluxes with He carrier gases were used for the O and N analysis, Sn flux with N_2 carrier gases for the H analysis, and W and Fe fluxes with O_2 carrier gases were used for the C analysis according to ASTM Standard E3346–22 [38]. From each synthesized alloy, three pieces were analyzed to minimize statistical variation.

2.3. Microstructural characterization and analysis

The phase composition of the as-cast RCCAs was assessed with a Rigaku SmartLab X-ray diffractometer (XRD) equipped with a Cu K_α ($\lambda = 0.1542$ nm) radiation source. Each XRD pattern was performed from 20° to 100° with a step size of 0.02° and speed of 2 steps per second. From the XRD patterns, the lattice parameters were extrapolated using the Nelson-Riley Method [39]. Analysis of the microstructural features of the as-cast RCCAs was performed using a FEI Quanta 3D field emission gun scanning electron microscope (SEM) equipped with a pole piece mounted backscatter electron (BSE) detector, an Everhart-Thornley secondary electron (SE) detector and an Oxford energy dispersive X-Ray spectrometer (EDS). The as-cast RCCAs were prepared such that all micrographs are viewed normal to the solidification direction, where the localized heating from the arc is at the top, and the surface of the RCCA in contact with the water-cooled Cu crucible is at the bottom. The samples were prepared for microstructural analysis by mounting in a conductive matrix mount and then mechanically polished up to 0.05 μm colloidal silica. The preferential mechanical polishing and slight etching from the colloidal silica enabled visualization of some grains and the boundaries between them.

Atom probe tomography (APT) was utilized to characterize and analyze the GB chemistry at the nanoscale of some selected RCCAs. The APT needles were prepared using a Ga focused ion beam (FIB) on a Zeiss Auriga 60 to lift out and sharpen a random GB from the as-cast RCCAs. The APT experiments were conducted in a Cameca Leap 4000X HR in laser probe mode at 55 K, using a pulse energy of 100 pJ, pulse rate of 125 kHz, and a target detection rate of 0.3 %. The APT measurement was reconstructed and analyzed using the Cameca AP Suite 6.3.1.110 software. To investigate the GB segregation of O observed via APT in the as-cast MoNbTaW RCCAs, the Langmuir-McLean isotherm, in Eq. (6) below was utilized [40–42].

$$\beta_i = \frac{X_i^{GB}}{X_i^{B}} = exp(-\frac{\Delta G_i^{GB}}{RT}) \tag{6}$$

Where β_i is the GB segregation coefficient, or GB enrichment factor, of the solute i, defined as the ratio of the concentration of the solute, i, at the GB, X_i^{GB}, to the concentration of the solute, i, in the bulk, X_i^{B}. R is the gas constant, T is the temperature at which the segregation occurs, and ΔG_i^{GB} is the segregation energy of component i. The Langmuir-McLean isotherm assumes that only a monolayer of solute is segregated to the GB and no distinct phases form [40–42]. Since the O content in the MoNbTaW RCCA is relatively dilute, and the GB can be treated as a separate and distinct thermodynamic state, this is a near-optimal method to analyze the segregation energy of O in the MoNbTaW RCCAs.

2.4. Ab initio modeling of the MoNbTaW GBs

To understand the formation of GB oxides based on their electronic structures, Density Functional Theory (DFT) method was employed to simulate O atom segregation to the MoNbTaW GBs and to understand the formation of GB oxides based on their electronic structures. DFT calculations were carried out using the Perdew-Burke-Ernzerhof (PBE) generalized-gradient approximation (GGA) functional [43] and the projector augmented wave approach [44] as implemented in the Vienna Ab initio Simulation Package (VASP v.6.3.2) [45]. Energy and forces were converged to at least 10^{-6} eV and 0.01 eV Å^{-1}, respectively. The BCC unit cell of MoNbTaW was built using the Special Quasirandom Structures (SQS) algorithm [46,47], and its Brillouin zone was sampled using a 8 × 8 × 4 Monkhorst-Pack ***k***-point grid and a kinetic energy cutoff of 450 eV [48,49]. We then relaxed the volume and cell dimensions of the unit cell to compute the lattice constant to be 3.218 Å, which is in a good agreement with experimentally measured lattice constant of 3.224 Å.

To model the GB, we have chosen Σ5 (001) as it is a low-angle grain boundary with a relatively low interfacial energy, which have been widely studied in several computational work on BCC GBs, including the NbMoTaW alloy in this work [50,51]. Our Σ5 (001) GB is modelled with dimensions of 40.7 Å x 20.4 Å x 6.5 Å (320 atoms) was created via the Aimsgb algorithm [41] using our previously determined lattice parameter of 3.218 Å with a 1 ×1×4 Monkhorst-Pack *k*-point grid and a kinetic energy cutoff of 450 eV (see the DFT benchmark plot in Supplementary Fig. SF3). GB models were simulated with three different compositions – denoted as APT, 65 Nb, and 55 Nb (see Table T1 in the Supporting Information). Atom positions of the metal elements were assigned at random throughout the supercell, and then swapped at the GB interface to produce Nb and Ta rich areas within 8 Å of the GB. Atom positions in the GB supercells were energetically minimized before inserting oxygen interstitials.

To model 7 at% O impurities in the grain boundary, 24 O atom atoms were randomly placed at the octahedral interstitial sites of the Σ5 (001) GB system. To capture the chemically and spatially diverse local environment of O atom interstitials within the GB, we simulated 11–19 configurations of the GB at a given alloy composition with varying O atom positions. This resulted in over 1100 unique O atom configurations with different local environments. The atomic coordination environment of each O atom interstitial defect in the GB was analyzed by counting the number of each element (Mo, Nb, Ta, W, O) within the nearest neighbor atoms of O atoms, which were defined with a cutoff radius of 3.2 Å.

O atom interstitial formation energy was calculated using a 16-atom, 2x2x1 supercell of bulk MoNbTaW (16 atoms) with a 3x3x3 Monkhorst-Pack *k*-point sampling and an energy cutoff of 450 eV (see the DFT benchmark plot in Supplementary Fig. SF2). The O atom interstitial formation energy (E_f) is defined by Eq. (7):

$$E_f = E_{bulk+O} - E_{bulk} - E_O \tag{7}$$

where E_{bulk+O} is the energy of the bulk with an O atom interstitial atom, E_{bulk} is the energy of the bulk, and E_O is the energy of a single O atom atom (which is half of the energy of an O atom molecule). Composition-dependent E_f values were computed by placing an O atom atom in an octahedral site and varying the composition of its six nearest neighbor metal atoms. For the two most abundant elements in the GB (Nb, Mo) as predicted by D. Aksoy, et al. [52,53], the electronic driving force for O atom interstitial formation was determined by computing the charge density difference ($\Delta\rho$) of O atom bonded to Nb and Mo as follows in Eq. (8):

$$\Delta\rho_{Nb-Mo} = \rho_{Nb} - \rho_{Mo} \tag{8}$$

where ρ_{Nb} (or ρ_{Mo}) is the electronic charge density of an O atom bonded to six Nb (or Mo) atoms in the 2x2x1 MoNbTaW supercell.

The O atom solubility limit in MoNbTaW was estimated using the same 16-atom supercell by increasing the O atom-to-metal atom ratio from 7 % (1 O to 16 metal atoms) to 33 % (8 O to 16 metal atoms). Five different configurations of the alloy were constructed at each O atom composition by randomly permutating the positions of refractory metal and O atom atoms within the supercell. Geometry optimization calculations were carried out for each configuration of the alloy containing O atoms to compute the O atom formation energy as a function of the O atom-to-metal ratio. From these data, the O atom solubility limit at T = 0 K was found to be the highest O atom concentration in which the alloy remained crystalline. The effect of temperature on the O atom solubility limit was predicted by taking the energy-minimized structures and then equilibrating those structures at T = 600 K using *ab initio* molecular dynamics (AIMD) simulations for 3 ps at the NVT ensemble using a Nose-Hoover thermostat and a time step of 2 fs [54]. The degree of crystallinity after adding O atoms to the alloy (i.e., % BCC) was analyzed using the polyhedral template matching method [55] as implemented in OVITO [56]. In the DFT and AIMD calculations, the chemical short-range order was taken into consideration by performing geometry optimization for a given local composition. Thermal equilibrium was achieved using AIMD simulations at 600 K. Additionally, local chemical fluctuations were accounted for by constructing multiple independent atomic models for a given GB composition.

3. Results

3.1. Synthesis of MoNbTaW RCCAs

The controlled PAM environments were utilized to synthesize 30 g ingots of the MoNbTaW RCCAs. Before synthesizing each RCCA, the partial pressures of the residual gases in the PAM chamber environments were measured using the quadrupole mass spectrometer and are shown below in Fig. 2a.

The total pressure in the PAM chamber before melting was 10 Torr, so relatively low contents of residual gases in the PAM chamber were observed, and the balance of the gases in the chamber was Ar, which is not plotted in Fig. 1a. With additional vacuum cycling and cleaning procedures, the contents of H_2O, O_2, N_2, and CO_2 residual gases in the PAM chamber are incrementally decreased. Residual H_2 gas content tends to remain steady across the PAM chamber environments, which may be due to its small size and mass.

From the measured residual gas contents in the PAM chamber environments, the thermodynamic equilibrium content of O and N in the MoNbTaW RCCAs was approximated using Eq. (1) for pure Nb [27–29]. The temperatures achieved during PAM were approximated using Eq. (5) with applied voltage and current of 30 V and 650 A, respectively, and a measured ingot radius of approximately 13 mm. Using Eq. (5), the approximate temperature achieved during arc melting was 4300 K. The predicted equilibrium contents of O and N at 4300 K, in each of the PAM chamber environments studied using the quadrupole mass spectrometer are plotted in Fig. 2b. The error bars are standard deviations from the variation in contents of O_2 and N_2 residual gas partial pressures in the PAM chamber environments. With higher O_2 and N_2 residual gas partial pressures detected in the PAM chamber, greater O and N interstitial impurities are expected in the as-cast RCCAs. MoNbTaW RCCAs were synthesized in the characterized PAM chamber environments for comparison with the equilibrium predictions.

In the controlled PAM chamber environments, 30 g MoNbTaW RCCA ingots were synthesized and the contents of interstitial impurities in the as-cast RCCAs were measured. In Fig. 2c, the contents of O, N, C, and H measured in the as-cast MoNbTaW RCCAs from each PAM chamber environment and feedstocks are depicted along with error bars for the standard deviation of the measured contents. In general, the MoNbTaW RCCAs synthesized using the commercial feedstocks had a range of 200 ppm O, a relatively large variation in the contents of interstitial impurities, much like in the feedstocks. They did not necessarily have

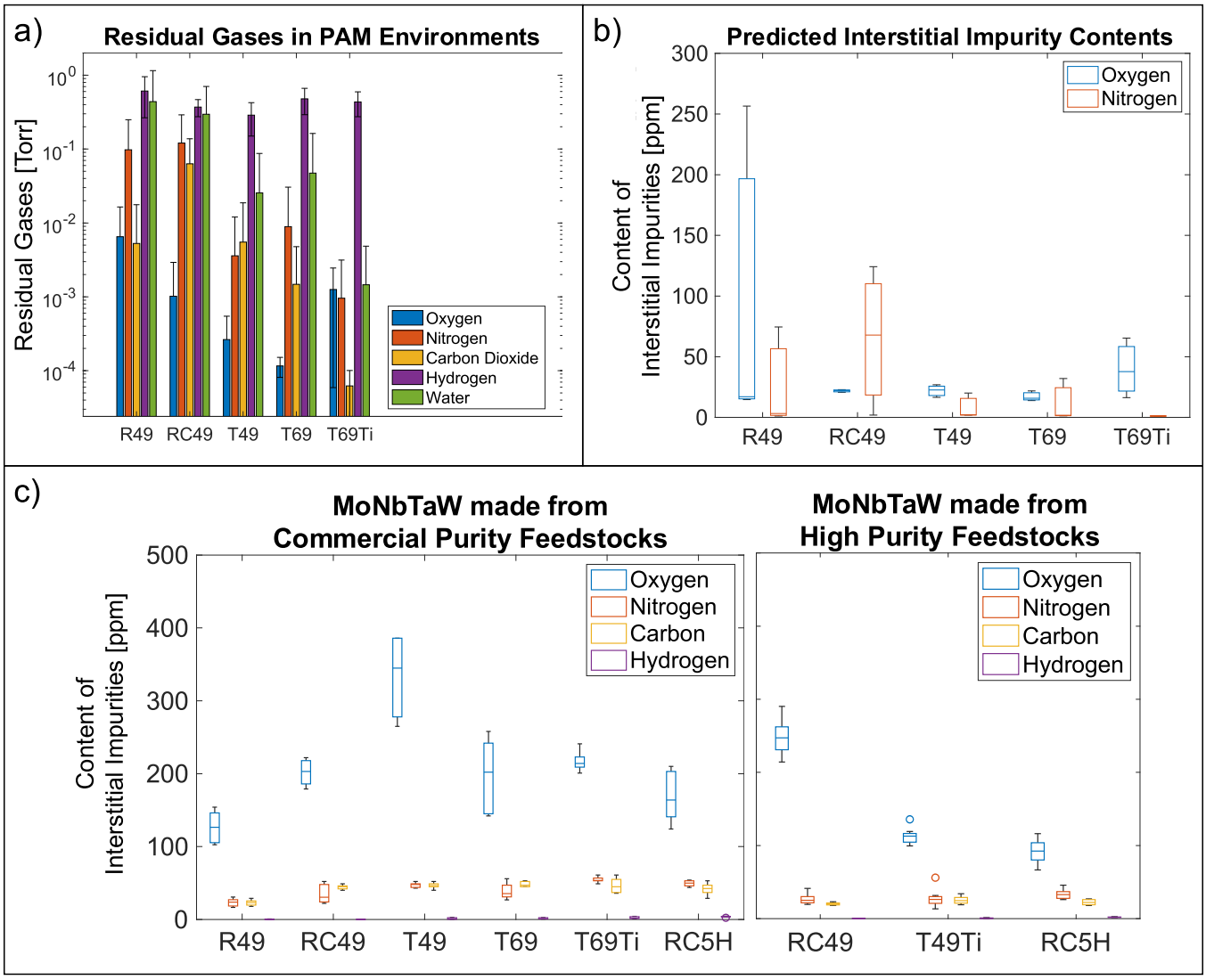

Fig. 2. (a) the partial pressures of the residual gases detected in the PAM chamber environments utilized for the synthesis of RCCAs, (b) equilibrium contents of O and N in alloys synthesized in the controlled PAM chamber environments, predicted using the equilibrium model for pure Nb, and (c) the actual contents of O, N, C, and H detected using IGF and CA in the as-cast MoNbTaW RCCAs synthesized from commercial purity and high purity feedstocks in the controlled PAM chamber environments.

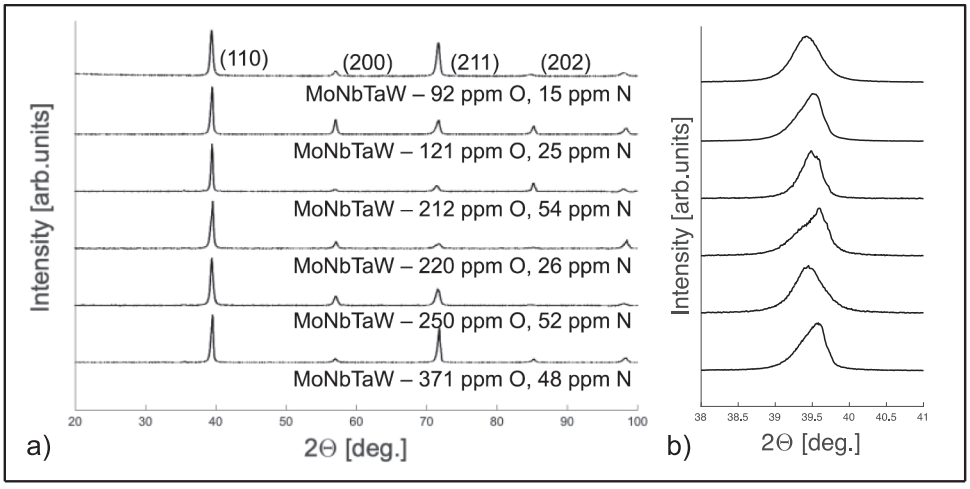

Fig. 3. XRD plots of the as-cast MoNbTaW RCCAs with (a) varying contents of interstitial impurities in the alloys and (b) plotted between 38° and 41° to reveal very little shift in peak position of the major (110) BCC peak, but some peak splitting into doublets.

fewer interstitial impurities with cleaner PAM chamber environments. The MoNbTaW RCCAs synthesized from the high-purity feedstocks had a range of ~ 100 ppm O, with smaller variations in the contents of interstitial impurities. They tended to have fewer interstitial impurities with improved PAM chamber environments. MoNbTaW RCCAs with ~ 90 ppm O were achieved by melting the high-purity feedstocks in the environment with 5 % H_2 forming gas, which could act as a reducing agent. To date, this is the lowest content of interstitial impurities studied in the MoNbTaW RCCA.

3.2. Microstructure and phases of the as-cast MoNbTaW RCCAs

Cross sections of as-cast MoNbTaW RCCAs with varying contents of O, N, C, and H were characterized by XRD to analyze the bulk crystalline structure, lattice parameters, and phase compositions. The XRD patterns of the as-cast MoNbTaW RCCAs with varying contents of interstitial impurities are shown below in Fig. 3a.

From the XRD patterns, all the as-cast MoNbTaW RCCAs appear to contain a single-phase BCC structure. Some of the RCCAs appear to have a small peak at ~ 35°, which may correspond to a TaO or NbO phase [57–61]. A closer inspection of the major XRD peak of each alloy is shown in Fig. 3b, plotted between 38° and 41° to reveal very little shift, less than 0.25° of the major (110) BCC peak. Some peak splitting is also observed in the XRD peaks in Fig. 3a–b, likely due to the segregation of elements during solidification and could vary with the slight variations in the sampling location from the bulk alloy. From the BCC peaks, the lattice parameters of the as-cast MoNbTaW RCCAs were extrapolated using the Nelson-Riley Method [39] and ranged between 0.3220 and 0.3230 nm.

To further investigate the microstructural features of the alloys and possible dendritic segregation, which may be indicated in some XRD peak splitting, the cross-section of an as-cast MoNbTaW RCCA with ~ 200 ppm O and 50 ppm N was analyzed via SEM. BSE and SE micrographs and corresponding EDS elemental maps are shown below in Fig. 4(a) and (b) from the top and bottom of the ingot, respectively.

From SEM BSE, SE, and EDS, regardless of the interstitial impurity content achieved in this study, the alloys appeared to have coarse, homogeneous grains near the bottom of the as-cast buttons, and solidification dendrites and micro-segregation near the top of the ingot which may have contributed to the observed XRD peak shift and splitting. The SEM BSE, SE, and EDS did not reveal any evidence of O, N, or C since these are light elements in relatively low concentrations, and no discernable oxide, nitride, or carbide phases were observed in SEM-EDS. The 30 g ingots were approximately 6 mm tall, and the lower 3 mm half contained the coarse, homogeneous grains, while the upper 3 mm half contained the segregated microstructure. For further investigation of the nanometer-scaled microstructural features resulting from the interstitial impurities in the MoNbTaW RCCAs, especially at the GBs, analysis is focused on the coarse, homogeneous grains near the bottoms of the as-cast ingots. Since GB segregation of interstitial impurities in the MoNbTaW RCCA is a known embrittling microstructural feature, a random GB from both a MoNbTaW RCCA with high content of interstitial impurities (250 ppm O, 52 ppm N) and low content of interstitial impurities (87 ppm O, 30 ppm N) were prepared for APT to probe the thermodynamic understanding of O and N segregation in the MoNbTaW RCCA. The GBs of the two alloys were prepared for APT using FIB as described in the methods and the sharpened APT needles containing the GBs are shown in Supplementary Fig. SF1.

The APT reconstructions of the GBs from the MoNbTaW RCCAs were used to investigate the nanometer scale microstructural features, resulting from the thermodynamic interactions between interstitial impurities, especially O, and the constituent refractory metal elements. APT reconstructions of the needles containing GBs are shown below in Fig. 5 with ions for Mo, Nb, Ta, and W hidden and NbO, TaO, O, N, and C ions visible for clarity.

In the APT reconstructions, cylindrical volumes containing the GB region and immediately adjacent regions of the abutting grains were constructed for compositional analyses of the GBs and are displayed in the reconstructions in Figures 5a1 and 5b1. No signals for carbides or nitrides were detected. 1D compositional profiles of the ion signals measured along the Z direction of the cylinders are also displayed in Figures 5a2 and 5b2. From the APT reconstruction and ion signal 1D profiles, evidence of O segregation and more specifically oxide formation at the GB is clear. For more detailed compositional analysis, the ion signal from the 1D compositional line profile of the cylinder was decomposed into the atomic concentrations of the elements in the MoNbTaW RCCAs across the GBs and shown in Figures 5a3 and 5b3. From the cylindrical volume, the average atomic concentrations of the

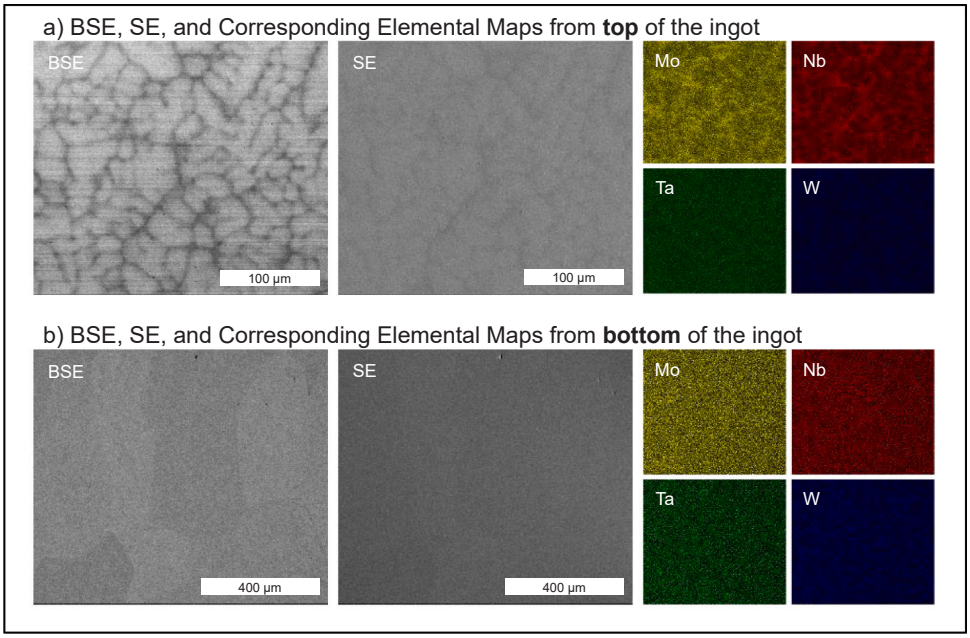

Fig. 4. BSE, SE and corresponding EDS elemental maps of the cross section of (a) the top and (b) the bottom of a MoNbTaW RCCA ingot with ~ 200 ppm O and ~ 50 ppm N, revealing coarse, homogeneous grains near the bottom of the ingot and solidification dendrites near the top of the ingot.

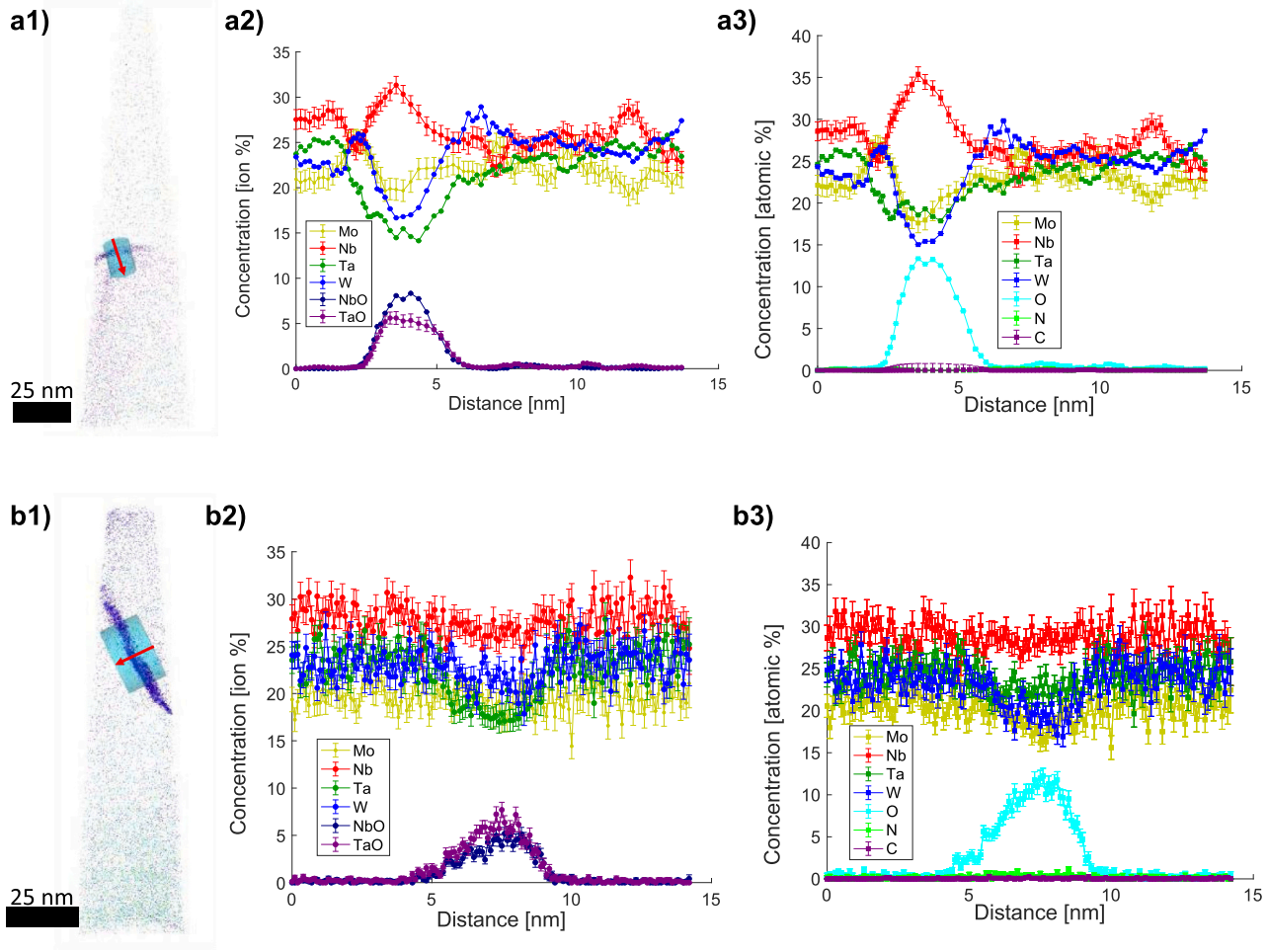

Fig. 5. APT reconstructions of the MoNbTaW RCCAs with (a1) 250 ppm O and (b1) 87 ppm O containing a random GB and cylindrical volumes constructed to analyze the chemistry at the GB and bulk regions of the alloys along with the (a2 and b2) ion signals across the GBs and the (a3 and b3) atomic concentrations from the decomposed ion signals across the GBs from the alloys.

elements in the bulk and the GB were determined and are listed below in Table 3.

From the decomposed ion signals of the volumes in the APT reconstructions, the atomic concentrations of the constituent metal elements, Mo, Nb, Ta, and W are near equiatomic in the bulk regions. The decomposed ion signals from the volumes in the APT reconstructions also revealed ~ 0.421 and 0.347 at% O in the bulk regions of the alloys is similar, but greater in magnitude compared to the 250 ppm O (0.215 at% O) and 87 ppm O (0.0751 at% O) measured by IGF. The decomposed ion signals from the GB regions revealed nearly 7 and 8 at% O to be segregated to the GBs in the MoNbTaW RCCAs. Additionally, the decomposed ion signals from the APT reconstructions of both MoNbTaW RCCAs, revealed a depletion of Mo, Ta, and W at the GB, with the largest differences observed in the depletion of Ta and W. The APT reconstruction of the MoNbTaW – 250 ppm O RCCA also revealed the enrichment of Nb at the GB, but little to no change in Nb concentration between the bulk and GB in the MoNbTaW – 87 ppm O RCCA. These results show that the segregation of O to GBs will proceed in the as-cast MoNbTaW RCCAs, even at extremely low bulk concentrations of O, and will still ultimately embrittle the alloy. Since O appears to be the most abundant and consequential interstitial impurity in the MoNbTaW RCCA; accordingly, the analysis will focus on O.

To understand the microscopic origin of O atom segregation to the GB and the formation of oxides in the GB determined from the APT measurements, Σ5 (001) GBs of MoNbTaW RCCA were simulated using DFT calculations. Three different GB models were constructed with varying compositions, denoted as “APT”, “65 Nb”, and “55 Nb” with 7 at % O in the GB. In the APT GB system, the constituent metal elements are uniformly distributed in space, according to the composition observed in the APT reconstruction of the MoNbTaW – 87 ppm O alloy, whereas in the 65 Nb and 55 Nb systems, the GB is enriched in Nb within the 0.8 nm-wide GB zone (see Fig. 6b-c). The Nb-rich compositions at the GB were simulated to study GB compositions predicted in recent classical Molecular Dynamics simulations which suggested that local chemical

Table 3
The atomic concentration of elements in the bulk and GB of the MoNbTaW RCCAs with varying contents of interstitial impurities, as measured in the volume constructed in the APT reconstruction.

Alloy	Location	Mo	Nb	Ta	W	O	N	C
MoNbTaW – 250 ppm O	Bulk	23.2	26.0	24.2	26.0	0.421	0.073	0.008
	GB	21.3	30.8	19.7	20.2	7.905	0.054	0.015
MoNbTaW – 87 ppm O	Bulk	21.0	28.9	24.6	24.5	0.347	0.167	0.030
	GB	19.4	28.5	23.1	21.4	6.693	0.381	0.073

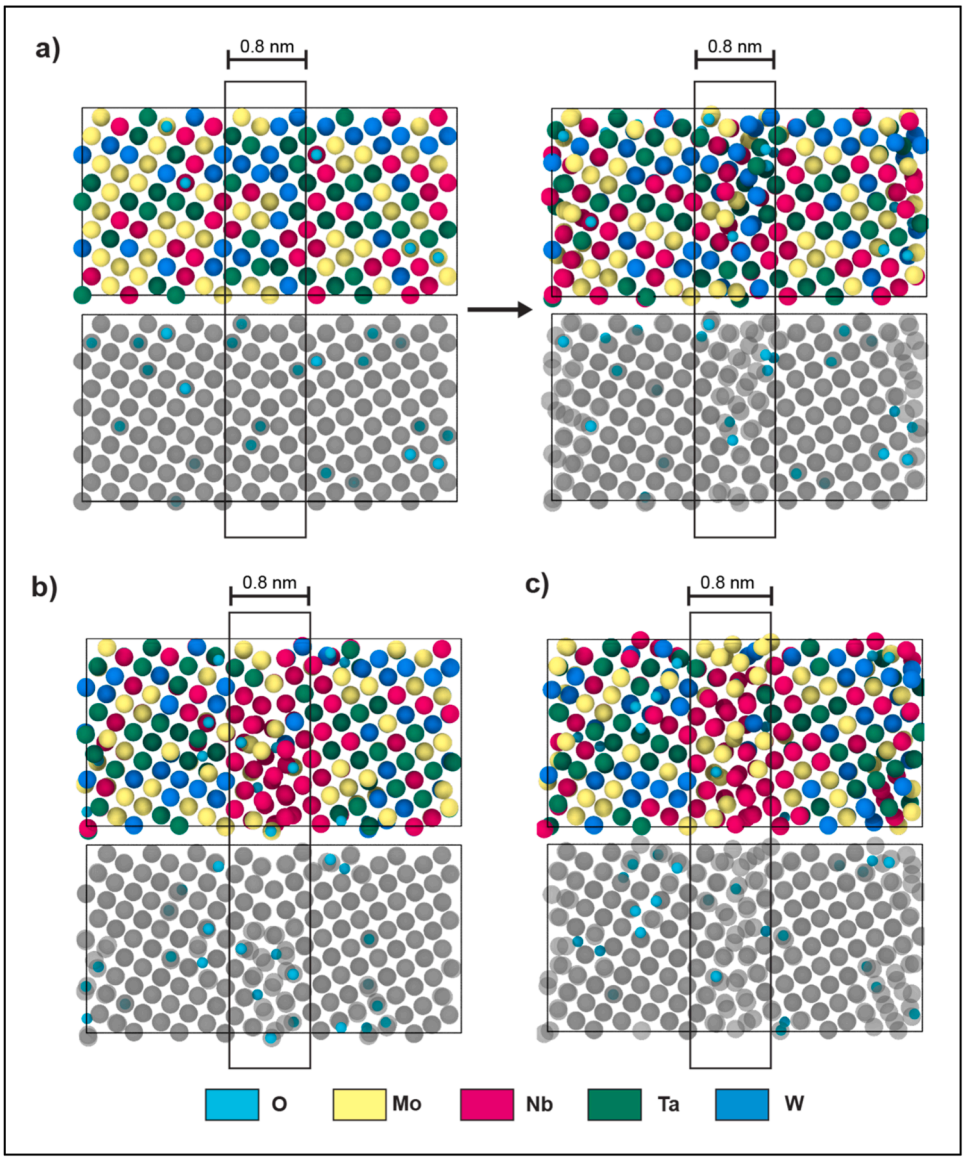

Fig. 6. Atomic models of the MoNbTaW bicrystal systems containing a Σ5 (001) GB and O interstitials (a) GB with the constituent metal composition observed in the APT reconstruction of the MoNbTaW – 87 ppm O alloy before (left) and after (right) the energy minimization of the GB structure using DFT calculations. (b-c) GB systems with (b) 65 at% Nb composition and (c) 55 at% Nb composition within the 0.8 nm-wide GB zone.

fluctuations and chemical short-range ordering in MoNbTaW drive Nb enrichment at the GB [52,53]. The 65 Nb bicrystal system was enriched with 65 at% Nb in the 0.8 nm wide GB region and the 55 Nb bicrystal system was enriched with 55 at% Nb at the GB. The exact atomic fraction of the constituent metal elements in the constructed bicrystals are detailed in Supplementary Table ST1. In each simulated GB, 7 at% O was added, as observed in the APT reconstructions.

From DFT calculations, the lattice parameter is approximated to be 0.3218 nm, which is in good agreement with the experimentally determined lattice parameters from XRD around 0.3220 nm in this work and similar to 0.3213 nm from previous literature [9]. Interestingly, some O atoms in the GB move away from their initial positions toward more favorable interstitial sites coordinated by Nb and Ta atoms. After geometry optimization, the 0.8 nm region in the GB becomes more structurally disordered in the presence of O atom atoms, shown in Fig. 6, suggesting there is an energetic driving force for atoms to move to more favorable coordination environments, dependent on local chemistry.

4. Discussion

4.1. Thermodynamic contributions to the origin of interstitial impurities

From the PAM synthesis of MoNbTaW RCCAs under varying conditions it is revealed that the thermodynamic drive for absorption or desorption of interstitial impurities controls the origin of interstitial impurities in the RCCAs. The thermodynamic contributors to the absorption or desorption of interstitial impurities can be characterized from the analysis of the experimental PAM synthesis of MoNbTaW RCCAs and the comparison of these results to predicted equilibrium contents of O in Nb. The discrepancies in the O content in the as-cast RCCAs and the thermodynamic equilibrium model predictions are useful for illustrating that the interstitial impurities in the feedstocks, competing residual gases in the PAM, the temperatures during PAM, and the constituent elements in the MoNbTaW RCCAs all govern the thermodynamic contributions to the absorption or desorption of O during PAM.

First, the chemistry and contents of the interstitial impurities in the

feedstocks utilized in the PAM synthesis of the RCCAs can drive the absorption or desorption of interstitial impurities into or out of the molten alloys during PAM. The feedstocks may begin with more or less than the equilibrium content of interstitial impurities of the alloy. This can be seen in the commercial and high purity feedstocks utilized in the synthesis of MoNbTaW RCCAs and the equilibrium contents of O and N predicted using Eqs. (1) and (2) for pure Nb, in Fig. 1a and 2b. Based on the calculated equilibrium levels of interstitial impurities, it is probable that the high purity feedstocks initially possessed interstitial impurity levels below equilibrium. For example, in the T49Ti PAM environment, the predicted equilibrium O content is on average ~180 ppm O, and up to ~300 ppm O, but the high purity Mo-W and Ta-Nb binary master alloy feedstocks started with ~70 and 100 ppm O, respectively. This lower interstitial impurity concentration could increase the thermodynamic driving force for the absorption of impurities from the PAM chamber into the molten RCCAs, made using high purity feedstocks. On the other hand, the commercial feedstocks started with ~140–250 ppm O, which exceeded the predicted equilibrium contents of interstitial impurities, especially compared to the T49, T69, and T69Ti PAM environments which had low partial pressures of residual O_2 gases. The RCCAs synthesized from commercial purity feedstocks in the PAM chambers with low partial pressures of O_2 residual gases, below ~10^{-3} Torr, may experience a stronger drive for the desorption of interstitial impurities in the form of diatomic gases. However, since the formation enthalpy of the individual oxides is far below zero, and the formation enthalpy of diatomic O_2 gas is 0 kJ/mol, atomic O may be driven to adsorb to the surface from the melt, but it is unlikely that it will form diatomic O_2 gas [25,26,32,62]. Instead, metal oxides may form and vaporize, or the O may absorb back into the molten alloy [62]. Furthermore, previous work has shown that evaporation of thermally unstable oxides and O absorption may occur simultaneously, resulting in little to no observable changes in the content of O impurities in the RCCAs, especially without the use of an ultra-high vacuum environment [29]. Without a separate, thermodynamically favorable reaction, such as a reduction reaction, O which begins in the feedstocks is not removed from the RCCAs during PAM. However, a broad range was observed from ~120 ppm O up to ~ 320 ppm O in the RCCAs made with commercial purity feedstocks. These broad ranges can be attributed to the starting commercial purity feedstocks, which also contained broad ranges of interstitial impurities, between 50 ppm O and 300 ppm O, and the O in the molten RCCAs cannot desorb from the RCCAs. Ultimately, the content of interstitial impurities in the starting feedstocks may

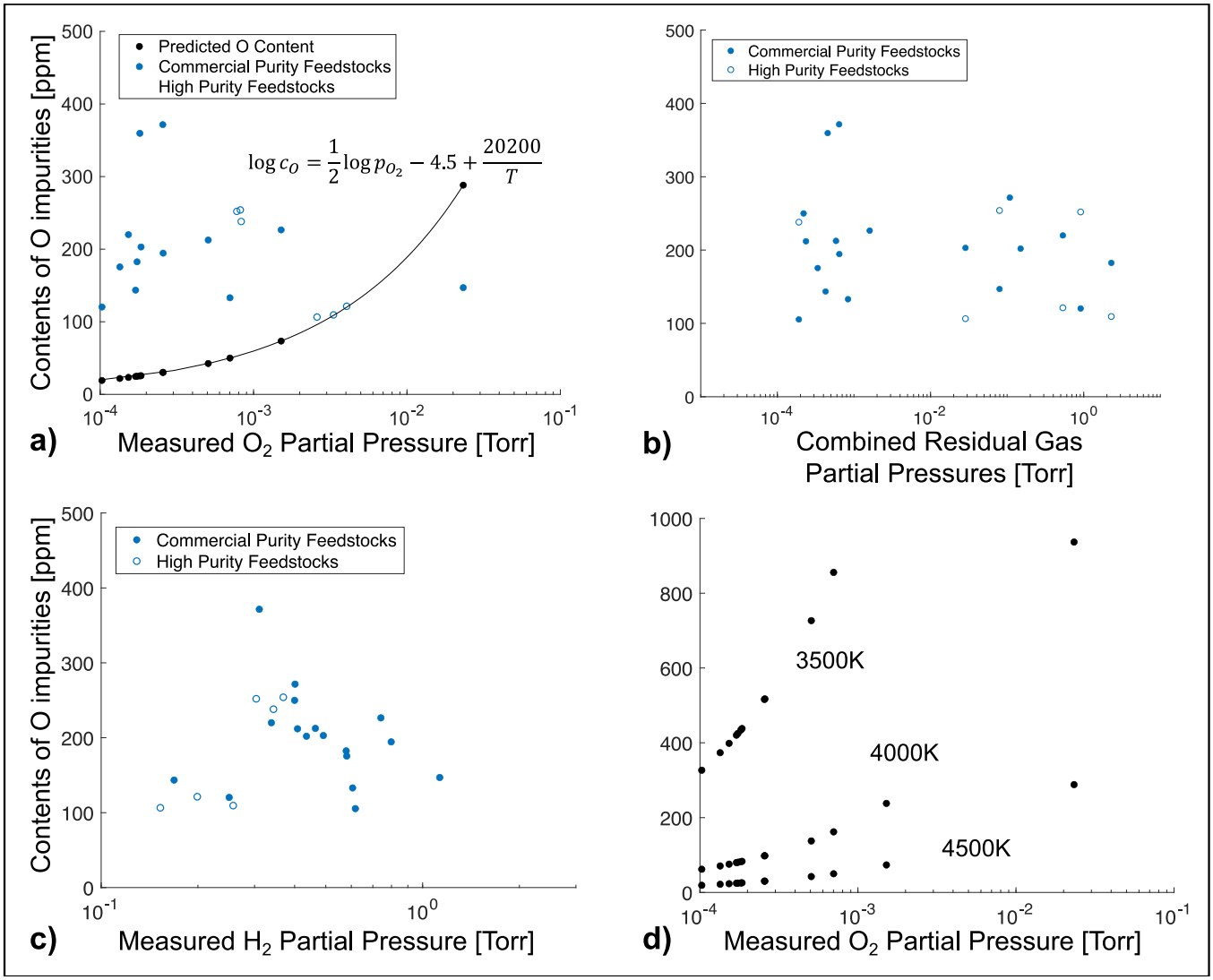

Fig. 7. The contents of O measured in the PAM synthesized MoNbTaW RCCAs (a) plotted along with the predicted equilibrium contents of O in Nb with respect to the measured partial pressures of O_2 in the PAM chamber environments, (b) plotted against the measured combined partial pressures of O_2, CO_2, and ½ H_2O in the PAM chamber environments, (c) plotted against the measured partial pressures of H_2 in the PAM chamber environments, as well as the (d) predicted equilibrium content of O in pure Nb at varied temperatures with respect to the measured partial pressures of O_2 in the PAM chamber environments.

dictate the minimum content of interstitial impurities in the RCCAs and significantly contributes to the origin of interstitial impurities since no desorption may occur during PAM synthesis. Feedstocks with low contents of interstitial impurities may drive the absorption of interstitial impurities from residual gases in the PAM environment. The residual gases will also affect interstitial impurities' absorption into the RCCAs.

In addition to the interstitial impurities in the feedstocks, both the chemistry and contents of the residual gases in the PAM chamber can govern the thermodynamic equilibrium content of interstitial impurities in the molten RCCAs and thus the drive for absorption or desorption of O. From the predicted equilibrium content of interstitial impurities in the alloys with different contents of O_2 in the PAM chamber, plotted in Fig. 2b, it is expected that as O_2 and N_2 partial pressures increase, the content of O and N in the as-cast RCCAs would also increase. The predicted equilibrium content of O in Nb, with respect to the measured partial pressures of O_2 is plotted along with the contents of interstitial impurities measured in all of the MoNbTaW RCCAs synthesized in this work, except those synthesized in the 5 % H_2 forming gas, in Fig. 7a below.

In Fig. 7a, it is clear that the measured contents of O impurities in the synthesized RCCAs do not correlate well with the measured partial pressures of O_2 in the PAM chamber environments. This is likely due to the contents of interstitial impurities in the starting feedstocks starting above the equilibrium content and cannot desorb or vaporize to approach equilibrium during PAM synthesis as discussed above [25,32,62]. The discrepancies in the O content in the as-cast RCCAs and the thermodynamic equilibrium model predictions are also due to other competing residual gases, but the equilibrium calculations only account for O_2 reactions with Nb. For example, H_2O or CO may also contribute O to the molten RCCAs and are governed by the reactions in Eqs. (9)-(11) below [29,63].

$$H_2O \quad (g) \leftrightarrow 2H \quad (l) + O \quad (l), \quad \Delta H^{\circ} \quad = 285 kJ/mol \tag{9}$$

$$CO(g) \leftrightarrow C \quad (l) + O \quad (l), \quad \Delta H^{\circ} \quad = 99 kJ/mol \tag{10}$$

$$CO_2 \quad (g) \leftrightarrow CO(g) + \frac{1}{2}O_2 \quad (g), \quad \Delta H^{\circ} \quad = 283 kJ \Big/ mol \tag{11}$$

From the reactions in Eqs. (9)-(11), it is possible that CO_2, CO, and H_2O can contribute interstitial O to the molten RCCAs, though significantly high temperatures are necessary to dissociate the gases into free, single atoms due to the energy required to dissociate the gases into atomic species which can adsorb to the surface of the molten metal. Furthermore, in the residual gas analysis, the CO was below the detectable limit of 10^{-12} Torr in the PAM chamber, so there is likely little contribution to O content in the RCCAs from CO. However, residual CO_2 contents detected in the PAM chamber could dissociate into CO gas and O atoms, which might contribute to O and C in the molten RCCAs·H_2O may also dissociate and can contribute H and O to the molten RCCAs. The additional reaction steps of the dissociation of H_2O and CO_2 to contribute O to pure molten alloys are poorly understood, and therefore cannot be easily predicted [27,29]. So in Fig. 7b, the measured O impurity content is plotted against the sum of the partial pressures of O_2, CO_2, and ½ H_2O to investigate the possible contributions from additional residual gases. If each of these residual gases converted to O_2 to then contribute O content to the molten RCCAs, then the relationship between the measured O content and the measured residual gases should follow an Arrhenius relationship, similar to the model plotted in Fig. 7a. However, it is clear that they do not, suggesting an additional mechanism may govern the contribution of interstitial impurities from the PAM chamber to the RCCAs. This may be due to thermodynamic stability of the reactions between residual gases in the PAM chamber.

As described by Eq. (9), residual H_2O gases in the PAM chamber may contribute a thermodynamic drive for absorption. Additionally, residual contents of H_2 can contribute a drive for the desorption of O from the molten RCCAs through the reverse, reducing redox reaction in Eq. (9) [26]. To investigate the contribution of H_2 to the thermodynamic drive for the desorption of O from the molten RCCAs, the content of O measured in the MoNbTaW RCCAs is plotted against the measured contents of H_2 residual gas in the PAM environment. In the data plotted in Fig. 7a–c, no H_2 gas was intentionally introduced into the PAM chamber, but H_2 is a challenging residual gas to control in vacuum chambers and environments due to its small size and mass, which make it difficult to remove, especially using vacuum pumps which rely on viscous flow [64,65]. Generally, as the residual H_2 gas content increased, the content of O in the molten RCCAs decreased. While quantitative thermodynamic models describing the reaction of H_2 with adsorbed O from a metal were not found, previous literature has shown the use of H_2 gas to reduce metal oxides and O impurities in various processes [66–69]. The data in Fig. 7c suggests residual H_2 may react with and drive the removal of O from the molten MoNbTaW RCCAs during PAM synthesis. The enthalpic drive for the reverse reaction in Eq. (9) is negative and can drive the reaction of residual H_2 with adsorbed O atoms. The residual H_2 can act as a reducing agent, contributing a thermodynamic drive for the desorption of and reaction with O, adsorbed to the molten alloy surface, forming H_2O gas, when the content of residual H_2O is relatively low [26]. The reducibility of H_2 is maintained when the ratio of H_2/H_2O is much greater than 1 [26]. Furthermore, residual H_2 may also react and neutralize residual O_2 in the chamber, forming H_2O as described in Eq. (9) [27,29]. To generalize the thermodynamic drive for the reduction of O from molten metals, Ellingham diagrams can be utilized to compare standard free energy (ΔG°) for the formation of H_2O to the ΔG° of the possible metal O atom reactions which may take place, in this case Mo-O, Nb-O, Ta-O, and W-O, at temperatures above 2000 K. In the MoNbTaW RCCA, at 2000 K, reactions of Nb-O have more negative $\Delta \boldsymbol{G}^{\circ}$, on the order of −480 kJ/mol than the reaction for the formation of H_2O which is on the order of −270 kJ/mol. However, at 2000 K some reactions, such as Mo-O, W-O, and Ta-O have more positive ΔG°, on the order of +49, −240, and −120 kJ/mol at 2000 K [26,70]. The residual H_2 gas and the relatively more positive ΔG° for Mo-O, W-O, and Ta-O reactions can drive the desorption of O from the MoNbTaW RCCA. Additionally, at extremely high temperatures, the reverse reaction in Eq. (10), to form CO, has a negative standard free entropy term (ΔS°) and thus becomes increasingly more stable at temperatures above 2000 K, with ΔG° on the order of −490 kJ/mol at 2000 K [26,70]. To take advantage of this control of thermodynamics, MoNbTaW RCCAs were also synthesized in the PAM chamber backfilled with Ar – 5 % H_2 forming gas, which produced a reducing environment, lowering the equilibrium content of O in the molten RCCAs. Furthermore, by replenishing the H_2 gas in the chamber after each flip and remelt, the ratio of H_2/H_2O was maintained far above 1. It resulted in MoNbTaW RCCAs with $<$ 100 ppm O, as shown in Fig. 2c and no evidence of H absorption into the MoNbTaW RCCA was observed.

The third contribution to the thermodynamic equilibrium content of O in the molten MoNbTaW RCCAs and thus the drive for absorption or desorption is the temperature achieved during PAM synthesis. The temperatures during PAM were roughly approximated by assuming the electrical power used to produce the arc entirely contributed to the superheated molten mixture of the MoNbTaW alloys in Eq. (5). The calculated temperature is only meant to provide a general range of the alloy melt temperature when molten during PAM. The temperature was roughly approximated to be 4300 K, and the predicted equilibrium contents of O and N at 4300 K were plotted in Fig. 2b. These approximated temperatures are consistent with those reported for arc melting processes [23,24]. To better understand the role of temperature in the thermodynamic drive for absorption of impurities, the predicted equilibrium contents of O for a range of temperatures and the measured partial pressures of O_2 in the PAM chamber environments are plotted in Fig. 7d. It is apparent the temperature of the molten RCCAs also controls the equilibrium content of O and thus the thermodynamic drive for

absorption or desorption. As the temperature of the molten RCCA decreases, the equilibrium content of O significantly increases and vice versa, but asymptotically approaches a minimum value. At lower temperatures, the equilibrium content significantly increases to ~ 300 ppm O, which would likely drive the absorption of O interstitial impurities into the molten RCCA. At extremely high temperatures, as illustrated by metal O atom Ellingham Diagrams, since most metal-oxide reactions have positive ΔS°, at extremely high temperatures, the formation of oxides and the absorption of O becomes less thermodynamically stable [26,70]. And as discussed previously, at extremely high temperatures, reactions to form H_2O and CO can become more stable than reactions to cause O absorption. During arc melting, although the top of the ingot, locally heated by the arc, is fully molten near 4300 K, the bottom of the ingot, which is in contact with the water-cooled Cu crucible, may be at a significantly lower temperature, near 300 K. Due to the localized heating and cooling, there is a significant thermal gradient across the RCCA ingot, which is ~ 10 mm tall and thus is likely at relatively low temperatures inside the RCCA ingot during synthesis. As observed in the SEM micrographs in Fig. 4b, the bottom of the RCCA ingot is possibly solid during the PAM process and therefore lower than the melting temperature (3100 K) of the MoNbTaW RCCA. This solid-state region which is at relatively low temperature may increase the equilibrium content of O in the molten RCCAs and drive absorption of O during PAM synthesis.

The last contributor to the thermodynamic equilibrium of interstitial impurity absorption or desorption in RCCAs during PAM synthesis is the chemistry and contents of the constituent metal elements in the RCCAs. In the MoNbTaW RCCA, Mo and W likely push the thermodynamic equilibrium content lower and drive less absorption due to their relatively less stable metal oxides which may vaporize and remove both Mo, W, and O from the alloys during melting at extremely high temperatures in the presence of O_2 compared to other refractory metals [29,32,33,62]. And as described previously, the ΔG° of the Mo-O and W-O are relatively less negative than those between Nb-O and Ta-O and can prevent the absorption of O interstitial impurities. On the other hand, transition metals used for RCCAs from subgroup IV and V tend to have much more negative ΔG° for O reactions thus stronger thermodynamic drive for absorption [26,70]. So RCCAs containing subgroup IV or V elements will face different thermodynamic constraints to prevent absorption of interstitial impurities since these elements have a stronger thermodynamic drive for absorption. For comparison, the contents of O, N, C, and H in the feedstocks and the as-cast NbTiZr RCCAs synthesized in the same characterized PAM environments utilized in the synthesis of MoNbTaW RCCAs are plotted below in Fig. 8a-b.

Similar trends in the as-cast NbTiZr RCCAs were observed in the MoNbTaW RCCAs, but the magnitude of the content of interstitial impurities in the as-cast RCCAs is significantly higher. Additionally, although the MoNbTaW RCCA could be degassed to some degree by using an Ar - 5 % H_2 reducing environment, the NbTiZr RCCA is more sensitive to the presence of H_2 gas in the PAM chamber. While no significant H_2 absorption was observed in the MoNbTaW RCCAs synthesized in the forming gas, reducing environments, the NbTiZr RCCAs absorbed significant amounts of H interstitial impurities, on the order of 220 ppm H, as shown in Fig. 8b. In the MoNbTaW RCCA, constituent elements such as Mo and W do not have a strong affinity for H or hydride formation, but Zr and Ti do have a strong affinity for H absorption [25, 62]. Furthermore, the equilibrium content model was originally developed for pure Nb not non-dilute alloys so the assumptions made to predict the absorption or desorption of O in RCCAs may only sometimes hold true as the development of RCCAs continues. Despite this, these models do work to some degree as a guiding framework for the synthesis of RCCAs in inert environment and vacuum processes. High purity MoNbTaW RCCAs with as low as 80 ppm O were achieved in this study using high purity feedstocks in a reducing Ar-H_2 environment; the highest purity MoNbTaW RCCAs published to date.

4.2. GB segregation and oxide formation in the MoNbTaW RCCA

From the microstructural investigations of the as-cast MoNbTaW RCCAs, there was significant evidence for forming GB oxides despite the relatively low content of O achieved in the RCCAs. In the XRD results shown in Fig. 3c, the lattice parameters of the as-cast RCCAs did not

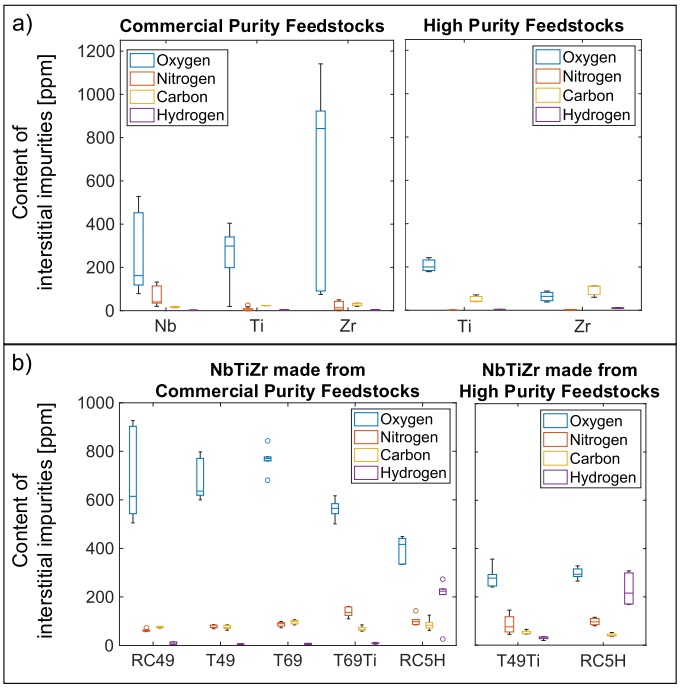

Fig. 8. The measured contents of interstitial impurities in the (a) feedstocks used to synthesize NbTiZr RCCAs as well as the (b) interstitial impurities in the NbTiZr RCCAs synthesized in the same conditions as the MoNbTaW RCCAs, revealing incremental changes to the contents of interstitial impurities and significant absorption of H from the Ar – 5 % H_2 forming gas reducing environments in addition the to the reduction of O from the RCCAs.

show consistent changes with respect to the contents of O. The formation of oxides at GBs in the MoNbTaW RCCAs, as evidenced by the APT results in Fig. 5, but were not detected in XRD led to imprecise assessment of the lattice parameter changes in the MoNbTaW RCCA. The additional peak at ~ 35° visible in some of the XRD patterns in Fig. 5a likely corresponds to the Nb- or Ta- oxide phase also detected in APT in the MoNbTaW RCCAs [57–61]. Thus far, the solubility limit of O in the MoNbTaW RCCA is not known. However, it is well known that O in pure Mo and pure W has no solubility and on the order of 1 at% O in pure Nb and pure Ta is soluble [71–75]. The observation of GB oxides in the APT reconstruction in Fig. 5b of the MoNbTaW RCCA with only 87 ppm O may suggest that the solubility limit of O is near 0, similar to pure Mo and pure W. Furthermore, below 100 ppm O, GB segregation in pure Mo and pure W can be avoided, the GBs can maintain cohesion, and the pure metals are reported to be ductile [34,35,76,77]. Below 100 ppm O, the MoNbTaW RCCA appears to undergo GB segregation of O still, embrittling the alloy. A low, but still unknown, solubility of O in the MoNbTaW RCCA may drive O segregation to GBs and may be governed by the enthalpic interactions between O and the individual constituent elements. Further analyses of the segregation and oxide formation energies are discussed.

The thermodynamic drive for GB segregation of O is further analyzed from the APT reconstruction and the constructed volumes containing the bulk and GB regions. Table 3 reports the decomposed contents of O in the bulk and GB of the MoNbTaW RCCAs. In the MoNbTaW – 250 ppm O RCCA, the content of O in the bulk and the GB was 0.421 and 7.905 at% O, respectively and in the MoNbTaW – 87 ppm O RCCA, the content of O in the bulk and GB was 0.347 and 6.693 at% O, respectively. Some slight enrichment of other elements (N and C) was also observed but APT detected no nitrides or carbides. Using the composition of O measured in the GB and in the bulk, and by treating the bulk and GB as distinct, separate thermodynamic states, the Langmuir-McLean Isotherm, Eq. (6), was used to approximate the GB segregation energy of O, ΔG_O^{GB}, in the MoNbTaW RCCAs. To determine the ΔG_O^{GB} in the MoNbTaW RCCAs, the temperature was assumed to be 3000 K, approximated from the possible thermal gradients in the RCCA during PAM synthesis, and were determined to be −73.14 kJ/mol in the MoNbTaW – 250 ppm O RCCA, and −73.81 kJ/mol in the MoNbTaW – 87 ppm O RCCA. The segregation energies of O from the APT measured GBs in the MoNbTaW RCCAs are similar in magnitude and appear to agree well with DFT literature which calculated similar order of magnitude segregation energies, approximately −144.72 kJ/mol [22]. Since there appears to be an oxide phase formed at the GB, and not a monolayer of O adsorbed at the GB surface, the Langmuir-McLean adsorption isotherm may not be a direct measure of the O segregation energy [40]. Nonetheless, there is a strong thermodynamic drive for the segregation of O in the MoNbTaW RCCA. Upon segregating to GBs, the enrichment of O at the GB and the formation of oxides, specifically NbO and TaO, may then proceed as detected in APT to form the most stable oxides. To investigate the GB oxide formation, the most stable oxides of the metal constituent elements found in the literature are listed in Table 4 below [71–75,78].

Nb and Ta which have the most negative oxide formation enthalpies drive the formation of oxides at the GB with the segregated O. W and Mo which have more positive formation enthalpies of their respective oxides and no solubility for O likely drive the segregation of O out of the solid solution matrix and into the GBs [73,75]. At the GB, the concentration of O reaches nearly 7 at% O, which is above the 1 at% O content threshold which drives oxide formation in pure Nb and Ta [71–75]. The thermodynamic drive for segregation and oxide formation is detrimental to the mechanical properties of the alloy, causing decohesion of the GBs and embrittling the RCCA [20,21]. It is well documented that the GB segregation of interstitial impurities and the formation of oxides at GBs in BCC alloys can disrupt the electron interactions at the GBs and lead to decohesion of the GB and embrittlement [34,79,80]. In Mo, alloying with Hf, or rare earth metals can cause the formation of oxides in the bulk and prevent GB segregation and embrittlement and segregation in W is prevented by achieving < 100 ppm O and in some cases alloying with Re [35,81–84]. In MoNbTaW, the constituent metal elements of the alloy likely drive the GB segregation and oxide formation and embrittlement of the RCCA. It is also possible that the local chemistry of the constituent metal elements may affect the drive for the formation of oxides at the GB.

Table 4
Enthalpies of formation, ΔH_f°, of the stable oxides of the constituent metal elements in the MoNbTaW RCCA, found in the literature [71–75,78].

Stable Oxides	ΔH_f° [kJ/mol]
MoO_3	−745
Nb_2O_5	−1899
WO_3	−842
Ta_2O_5	−2045

To understand the chemical driving forces for O segregation and oxide formation in the GB at the atomic level, the local O coordination environment was sampled from over a thousand configurations using DFT calculations. The displacement-coordination maps of O atom populations are shown in Supplementary Fig. SF4. From DFT, the local the local chemistry-dependent O atomic mobility is visualized below in Fig. 9.

O atoms on average tend to diffuse towards Nb and Ta atoms, indicated by $\Delta N_O > 0$ for Nb and Ta with increasing displacement d, to minimize the total energy of the GB. Simultaneously, these O atoms move away from Mo and W (i.e., $\Delta N_O < 0$ for Mo and W). These results are consistent with experimental findings of NbO and TaO in the alloy GB from APT measurements, suggesting that O diffuses to energetically favorable coordination environment consisting of Nb and Ta atoms as shown in Fig. 9a. Surprisingly, we find similar trends of O moving towards Nb and Ta across all GB models, regardless of their atomic compositions. To verify this, we computed the % local atomic composition averaged over all mobile O atoms that moved more than half of the lattice constant ($d > 0.15$ nm). As seen in Fig. 9b–c, there is a net increase in the number of Nb and Ta atoms after energy minimization via O displacement. O may preferentially diffuse toward sites with more Nb and Ta in the local chemical environments in the MoNbTaW RCCA.

The energetic driving force for O atom movement towards a preferential chemical environment was then quantified by calculating the O interstitial formation energy (E_f) with varying nearest neighbors of O atoms. The interstitial formation energy is the lowest when O is bonded to Nb and Ta, with E_f of –2.80 eV and –3.06 eV, respectively, compared to Mo and W with E_f of –1.11 eV and –0.37 eV, respectively (see Supplementary Table ST2). A greater extent of charge transfer from an O atom to a metal atom lowers the interstitial O atom formation energy and induces oxide formation. From analysis of the charge density difference, a larger local electron density near Nb, where O preferentially bonded was observed, suggesting that O prefers to transfer its electrons to Nb compared to Mo. There is as much as a 2 eV stronger driving force for O to prefer local chemical environments rich with Nb and Ta as opposed to environments rich with Mo and W. In the MoNbTaW RCCA, the preference for O to occupy sites near Nb and Ta, as opposed to Mo and W in the alloy can drive the segregation of O to the GB. Once segregated to the GB, O contents above 1 at%, can then lead to the formation of Nb- and Ta- oxides. Furthermore, previous MD simulations have predicted that there is a driving force for the enrichment of Nb and the depletion of W and Ta at and around the GB in the MoNbTaW RCCA [52,53]. This predicted enrichment of Nb at the GB can further drive the segregation of O and the formation of oxides at the GB, as revealed by the DFT results in Fig. 9b – c. The enrichment of Nb and O at the GB may also enhance the formation of oxides at the GB due to the relatively low enthalpy of formation for Nb-oxides. These findings along with the observed experimental results of this work suggest that especially with the presence of GBs, there is very little solubility of O in the MoNbTaW

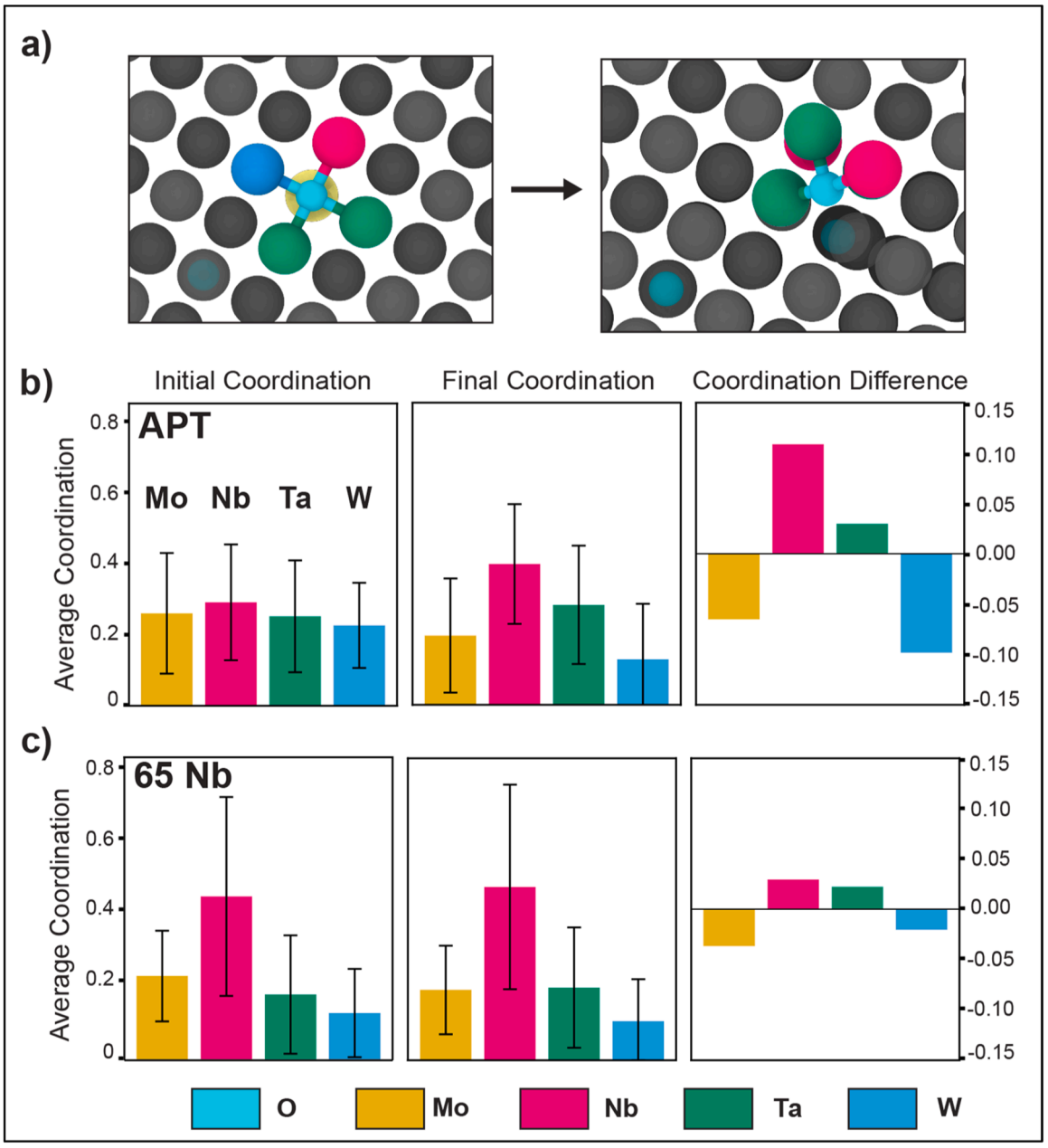

Fig. 9. Local chemistry-dependent O atomic mobility from DFT. (a) Representative snapshots of the O coordination environment before (left) and after (right) geometry optimization. (b,c) Percent compositions of the initial, final, and difference in the coordination environment of mobile O atoms (with $d > 0.15$ nm) in the APT and 65 Nb GB systems, respectively. Statistics are averaged over ~1100 O atom configurations with standard deviations reported as error bars.

RCCA, possibly below the contents of O achieved in this study.

In the MoNbTaW RCCA supercells of 320 atoms, containing a Σ5 (001) GB and 7 at% O, it was found that in all configurations, the addition of O reduced the stability of the BCC structure. The supercells started with only 25 % of the atoms in a disordered structure, to model the GB, and in all configurations, with the addition of O, the relaxed supercell structure contained more than 25 % of the atoms in a disordered structure. This suggests there is a driving force for O to prefer sites with more coordination preference and that there is little solubility of O in the MoNbTaW RCCA, especially in the presence of a GB. So, a monocrystal of the BCC MoNbTaW RCCA containing 16 atoms per supercell was constructed to investigate the solubility of O in the BCC crystal structure of the MoNbTaW RCCA using DFT calculations. At only 1 O atom in the supercell, or 6 at% O, no change in structural stability was observed, and the theoretical upper bound of O solubility limit in the alloy was estimated to be nearly ~20 at% O at $T = 0$ K (see Supplementary Fig. SF6a). To account for the temperature effects on the solubility limit, AIMD simulations were conducted at a higher temperature. Dynamical simulations showed that the alloy is less structurally stable with more O atoms and higher thermal energy (see Supplementary Fig. SF6b), suggesting that the solubility limit decreases at temperatures closer to room temperature. This indicates that the GBs in the MoNbTaW RCCA, may provide a lower energetic landscape for segregation of O. It is possible that without the presence of GBs in the MoNbTaW, there may be a measurable solubility limit of O in the alloy. Furthermore, in a single crystal of the MoNbTaW RCCA, it is possible that local chemical fluctuations of Nb, Ta, Mo, and W, could allow O to sit in preferential interstitial sites near Nb and Ta elements. Realistically, it is not likely that even a single crystal of the MoNbTaW RCCA has as much as 6 at% O solubility, but there may be some O solubility in the MoNbTaW RCCA. However, in the presence of GBs, O will segregate due to the low coordination and relatively high enthalpic interaction O has

with Mo and W in the alloy.

In the MoNbTaW RCCA, interstitial impurities, such as O, can be controlled to some degree through processing. However, additional alloy design strategies are necessary to develop an alloy from this RCCA family with high strength at elevated temperatures and ductility at room temperature. Mo and W may cause the solid solubility of O in the RCCA to be extremely low, driving the segregation of O to the GBs. At the GBs, the enrichment of O will then lead to the formation of stable oxides at the GB. So, the presence of Nb and Ta in the MoNbTaW RCCA may assist the detrimental oxide formation in the RCCA since Nb- and Ta- oxides are so relatively stable. Nb and Ta have such low oxide formation enthalpies as well as relatively high local electron densities compared to Mo and W, O will very readily segregate to GBs and form oxides and thus a lower limit of O to prevent GB segregation was not achieved in this study. These competing enthalpic interactions between all the constituent elements with O and the different local electron densities of the constituent elements can drive O GB segregation and oxide formation even at concentrations below 100 ppm O as displayed in this work. Unlike pure Mo and W, O content limits far below 100 ppm may be necessary to achieve MoNbTaW RCCAs without GB segregation and oxide formation. Such extremely low O contents in the MoNbTaW RCCA may be required that the use of conventional PAM techniques may not be able to achieve MoNbTaW RCCAs with room temperature ductility. More advanced processing techniques to further minimize O content or to achieve single crystal MoNbTaW RCCAs may be necessary. Furthermore, alloy design techniques must consider these enthalpic interactions to develop MoNbTaW based RCCAs which do not undergo severe GB segregation oxide formation. Because Mo and W will push O to segregate to GBs at even very low concentrations, and Nb and Ta will strongly drive the formation of oxides, especially at GBs, constituent elements like Ti or Hf which improve O solubility and can scavenge O from the GBs are necessary to further design MoNbTaW based RCCAs.

5. Conclusions

This work has provided thermodynamic insight into the origin and formation of interstitial impurities in the MoNbTaW RCCA. This information should be helpful for the processing and design of future RCCAs. Thermodynamic equilibria can be utilized to drive the absorption or desorption of interstitial impurities, such as O during the synthesis of RCCAs as well as for improved refractory alloy design to avoid detrimental O segregation and oxide formation. The key conclusions from this study for the synthesis and design of RCCAs, by considering thermodynamic equilibria are detailed below.

- During PAM, the content of interstitial impurities in RCCAs are governed by the thermodynamic equilibria between the identities and contents of interstitial impurities in the feedstocks, residual gases in the environment, the identities of the constituent metals in the molten alloys, and the temperature of the molten RCCAs, as already established in pure BCC metals.
- A reducing environment can be used to degas O from the molten RCCAs since the dissociation of O_2 into individual O atoms is not a reversible reaction and was used in combination with high purity feedstocks to produce the highest purity MoNbTaW RCCAs published to date.
- APT measurements and DFT simulations of the MoNbTaW alloy revealed that despite the low contents of O achieved in the MoNbTaW RCCAs in this study, the local charge distributions of the individual constituent elements and the preferential segregation of Nb to GBs collectively drives the segregation of interstitial impurities, especially O, and the formation of oxides at GBs.

However, it is clear current equilibrium models of the absorption of O and N in pure metals such as Nb may not accurately describe the absorption of those same interstitial impurities into non-dilute solutions of refractory metal alloys. Though general approximations and primary contributors are known, the exact contributions of the sources of interstitial impurities into RCCAs is still not precisely quantified. The processing pathways as well as the compositional design of RCCAs must be carefully considered synergistically to develop RCCAs with high strength at elevated temperatures and ductility at room temperature. Interstitial impurities, especially O, can have a strong thermodynamic preference to segregate to GBs in MoNbTaW, driven by low solubilities and high enthalpies of oxide formation with the constituent elements. At the GB, enrichment of O and certain constituent elements, such as Nb, can lead to the formation of detrimental oxides and severe embrittlement of the RCCA. Constituent elements that combat O segregation must be added to RCCAs with intention to improve their sensitivity to interstitial impurities.

CRediT authorship contribution statement

Benjamin MacDonald: Writing – review & editing, Validation, Supervision, Methodology, Conceptualization. **Elizabeth Lee:** Writing – review & editing, Validation, Supervision, Software, Resources, Methodology, Project Administration, Conceptualization, Funding acquisition. **Delphine Chassaing:** Visualization, Methodology, Investigation. **Torben Boll:** Writing – review & editing, Validation, Supervision, Resources, Project administration, Methodology, Investigation, Funding acquisition. **Sydney To:** Writing – review & editing, Writing – original draft, Visualization, Validation, Methodology, Formal analysis, Data curation, Investigation. **Yemao Lu:** Writing – review & editing, Validation, Methodology, Investigation, Data curation. **Daisy Kamp:** Writing – review & editing, Writing – original draft, Visualization, Validation, Software, Methodology, Investigation, Formal analysis. **Calvin Belcher:** Writing – original draft, Visualization, Validation, Methodology, Investigation, Formal analysis, Data curation, Conceptualization. **Diran Apelian:** Writing – review & editing, Supervision, Resources, Project administration, Investigation, Funding acquisition, Conceptualization. **Enrique Lavernia:** Writing – review & editing, Validation, Supervision, Resources, Project administration, Investigation, Funding acquisition, Conceptualization.

Declaration of Competing Interest

The authors declare the following financial interests/personal relationships which may be considered as potential competing interests: Calvin Belcher reports financial support, article publishing charges, and travel were provided by National Science Foundation Division of Materials Research. If there are other authors, they declare that they have no known competing financial interests or personal relationships that could have appeared to influence the work reported in this paper.

Acknowledgements

The authors would like to acknowledge Paul Aimone and Dave Smathers from Materion for their generous donation of feedstock materials for this work. The authors would also like to thank Cesar Ballestar, Andrew Lin, Ashlee Phillips, and Georg Schick from Verder Scientific for their assistance in the IGF measurements. This research was primarily supported by the National Science Foundation Materials Research Science and Engineering Center, Division of Materials Research through the UC Irvine Center for Complex and Active Materials (DMR-2011967). The authors acknowledge the use of facilities and instrumentation at the UC Irvine Materials Research Institute (IMRI) supported in part by the National Science Foundation Materials Research Science and Engineering Center program through the UC Irvine Center for Complex and Active Materials (DMR-2011967). This work was partly carried out with the support of the Karlsruhe Nano Micro Facility (KNMF, www.knmf.kit.edu), a Helmholtz Research Infrastructure at Karlsruhe Institute of Technology (KIT, www.kit.edu).

This work utilized the infrastructure for high-performance and high-throughput computing, research data storage and analysis, and scientific software tool integration built, operated, and updated by the Research Cyberinfrastructure Center (RCIC) at the University of California, Irvine. The RCIC provides cluster-based systems, application software, and scalable storage to directly support the UCI research community. https://rcic.uci.edu.

Appendix A. Supporting information

Supplementary data associated with this article can be found in the online version at doi:10.1016/j.jallcom.2024.177520.

Data availability

Data will be made available on request.

References

[1] E.P. George, D. Raabe, R.O. Ritchie, High-entropy alloys, Nat. Rev. Mater. 4 (2019) 515–534, https://doi.org/10.1038/s41578-019-0121-4.
[2] O.N. Senkov, D.B. Miracle, S.I. Rao, Correlations to improve room temperature ductility of refractory complex concentrated alloys, Mater. Sci. Eng.: A (2021), https://doi.org/10.1016/j.msea.2021.141512.
[3] F. Wang, G.H. Balbus, S. Xu, Y. Su, J. Shin, P.F. Rottmann, K.E. Knipling, J. C. Stinville, L.H. Mills, O.N. Senkov, I.J. Beyerlein, T.M. Pollock, D.S. Gianola, Multiplicity of dislocation pathways in a refractory multiprincipal element alloy, Science (1979) 370 (2020) 95–101, https://doi.org/10.1126/science.aba3722.
[4] J. Pang, H. Zhang, Y. Ji, Z. Zhu, L. Zhang, H. Li, A. Wang, H. Zhang, High-temperature structural and mechanical stability of refractory high-entropy alloy Nb40Ti25Al15V10Ta5Hf3W2, Mater. Charact. 205 (2023), https://doi.org/10.1016/j.matchar.2023.113321.
[5] J. Pang, H. Zhang, L. Zhang, Z. Zhu, H. Fu, H. Li, A. Wang, Z. Li, H. Zhang, A ductile Nb40Ti25Al15V10Ta5Hf3W2 refractory high entropy alloy with high specific strength for high-temperature applications, Mater. Sci. Eng.: A 831 (2022) 142290, https://doi.org/10.1016/j.msea.2021.142290.
[6] Z. Li, J. Pang, H. Liu, Z. Zhu, L. Zhang, A. Wang, W. Li, H. Zhang, H. Zhang, Combined effect of silicon doping and thermal treatment on microstructures and mechanical properties of Ti50Nb20V20Al10 refractory high-entropy alloy, J. Alloy. Compd. 1005 (2024) 176075, https://doi.org/10.1016/j.jallcom.2024.176075.
[7] O.N. Senkov, D.B. Miracle, S.I. Rao, Correlations to improve room temperature ductility of refractory complex concentrated alloys, Mater. Sci. Eng.: A (2021), https://doi.org/10.1016/j.msea.2021.141512.
[8] O.N. Senkov, S. Gorsse, D.B. Miracle, High temperature strength of refractory complex concentrated alloys, Acta Mater. 175 (2019) 394–405, https://doi.org/10.1016/j.actamat.2019.06.032.
[9] O.N. Senkov, G.B. Wilks, D.B. Miracle, C.P. Chuang, P.K. Liaw, Refractory high-entropy alloys, Intermetallics (Barking) 18 (2010) 1758–1765, https://doi.org/10.1016/j.intermet.2010.05.014.
[10] O.N. Senkov, G.B. Wilks, J.M. Scott, D.B. Miracle, Mechanical properties of Nb25Mo25Ta 25W25 and V20Nb20Mo 20Ta20W20 refractory high entropy alloys, Intermetallics (Barking) 19 (2011) 698–706, https://doi.org/10.1016/j.intermet.2011.01.004.
[11] O.N. Senkov, J.M. Scott, S.V. Senkova, D.B. Miracle, C.F. Woodward, Microstructure and room temperature properties of a high-entropy TaNbHfZrTi alloy, J. Alloy. Compd. 509 (2011) 6043–6048, https://doi.org/10.1016/j.jallcom.2011.02.171.
[12] Z. Lei, X. Liu, Y. Wu, H. Wang, S. Jiang, S. Wang, X. Hui, Y. Wu, B. Gault, P. Kontis, D. Raabe, L. Gu, Q. Zhang, H. Chen, H. Wang, J. Liu, K. An, Q. Zeng, T.G. Nieh, Z. Lu, Enhanced strength and ductility in a high-entropy alloy via ordered oxygen complexes, Nature 563 (2018) 546–550, https://doi.org/10.1038/s41586-018-0685-y.
[13] Y.X. Ye, B. Ouyang, C.Z. Liu, G.J. Duscher, T.G. Nieh, Effect of interstitial oxygen and nitrogen on incipient plasticity of NbTiZrHf high-entropy alloys, Acta Mater. 199 (2020) 413–424, https://doi.org/10.1016/j.actamat.2020.08.065.
[14] R. Wang, Y. Tang, Z. Lei, Y. Ai, Z. Tong, S. Li, Y. Ye, S. Bai, Achieving high strength and ductility in nitrogen-doped refractory high-entropy alloys, Mater. Des. 213 (2022) 110356, https://doi.org/10.1016/j.matdes.2021.110356.
[15] Z. Lei, Y. Wu, J. He, X. Liu, H. Wang, S. Jiang, L. Gu, Q. Zhang, B. Gault, D. Raabe, Z. Lu, Snoek-type damping performance in strong and ductile high-entropy alloys, Sci. Adv. 6 (2020) 1–9, https://doi.org/10.1126/sciadv.aba7802.
[16] M. Jiao, Z. Lei, Y. Wu, J. Du, X.Y. Zhou, W. Li, X. Yuan, X. Liu, X. Zhu, S. Wang, H. Zhu, P. Cao, X. Liu, X. Zhang, H. Wang, S. Jiang, Z. Lu, Manipulating the ordered oxygen complexes to achieve high strength and ductility in medium-entropy alloys, Nat. Commun. 14 (2023) 1–11, https://doi.org/10.1038/s41467-023-36319-0.
[17] C. Jin, X. Li, J. Kang, H. Li, H. Wang, Effect of interstitial oxygen /nitrogen on mechanical and wear properties of TiZrHfNb refractory high-entropy alloy, J. Alloy. Compd. 960 (2023) 170863, https://doi.org/10.1016/j.jallcom.2023.170863.
[18] X. Li, H. Li, Q. Li, C. Jin, K. Hua, H. Wang, The determining role of Al addition on tribology properties and oxidation behavior at elevated temperatures of TiZrHfNb refractory high-entropy alloy, Mater. Charact. 189 (2022) 111921, https://doi.org/10.1016/j.matchar.2022.111921.
[19] H. Li, X. Li, C. Jin, Q. Li, Q. Ma, K. Hua, H. Wang, W. Liu, Mechanical and tribological performance of AlCr0.5NbTaxTi4–x (x = 0, 0.5, 1) refractory high-entropy alloys, J. Mater. Sci. Technol. 156 (2023) 241–253, https://doi.org/10.1016/j.jmst.2023.02.016.
[20] Y. Zou, P. Okle, H. Yu, T. Sumigawa, T. Kitamura, S. Maiti, W. Steurer, R. Spolenak, Fracture properties of a refractory high-entropy alloy: in situ micro-cantilever and atom probe tomography studies, Scr. Mater. 128 (2017) 95–99, https://doi.org/10.1016/j.scriptamat.2016.09.036.
[21] Y. Zou, S. Maiti, W. Steurer, R. Spolenak, Size-dependent plasticity in an Nb25Mo25Ta 25W25 refractory high-entropy alloy, Acta Mater. 65 (2014) 85–97, https://doi.org/10.1016/j.actamat.2013.11.049.
[22] Z. Wang, H. Wu, Y. Wu, H. Huang, X. Zhu, Y. Zhang, H. Zhu, X. Yuan, Q. Chen, S. Wang, X. Liu, H. Wang, S. Jiang, M.J. Kim, Z. Lu, Solving oxygen embrittlement of refractory high-entropy alloy via grain boundary engineering, Mater. Today 54 (2022) 83–89, https://doi.org/10.1016/j.mattod.2022.02.006.
[23] R. Knight, R.W. Smith, D. Apelian, Application of plasma arc melting technology to processing of reactive metals, Int. Mater. Rev. 36 (1991) 221–252, https://doi.org/10.1179/imr.1991.36.1.221.
[24] Gruber Helmut, Consumable-electrode vacuum arc melting, J. Met. (1958) 193–198, https://doi.org/10.1201/9781315221618-6.
[25] J.D. Fast, Interaction of Metals and Gases Vol. 1 Thermodynamics and Phase Relations, Academic Press, New York, 1965.
[26] H.J.T. Ellingham, Reducibility of oxides and sulphides in metallurgical processes, J. Soc. Chem. Ind. Trans. Commun. 63 (1944) 125–160, https://doi.org/10.1002/jctb.5000515215.
[27] E. Fromm, Gas-metal reactions of refractory metals at high temperature in high vacuum, J. Vac. Sci. Technol. 7 (1970) S100–S105, https://doi.org/10.1116/1.1315891.
[28] H.J. Grabke, G. Horz, Kinetics and mechanisms of gas-metal interactions, Annu. Rev. Mater. Sci. 7 (1977) 1057–1076.
[29] E. Fromm, H. Jehn, Thermodynamics and phase relations in refractory metal solid solutions containing carbon, nitrogen, and oxygen, Metall. Trans. 3 (1972) 1685–1692, https://doi.org/10.1007/BF02642547.
[30] C.H. Belcher, B.E. MacDonald, D. Apelian, E.J. Lavernia, The role of interstitial constituents in refractory complex concentrated alloys, Prog. Mater. Sci. 137 (2023) 101140, https://doi.org/10.1016/j.pmatsci.2023.101140.
[31] J. Liu, B.S. Li, H. Gardner, Y. Gong, F. Liu, G. He, M. Moorehead, C. Parkin, A. Couet, A.J. Wilkinson, D.E.J. Armstrong, Origin of age softening in the refractory high-entropy alloys, Sci. Adv. 9 (2023) 1–11, https://doi.org/10.1126/sciadv.adj1511.
[32] J.D. Fast, Interaction of Metals and Gases: Kinetics and Mechanisms, Macmillan, 1972.
[33] E. Fromm, G. Hörz, Hydrogen, nitrogen, oxygen, and carbon in metals, Int. Met. Rev. 25 (1980) 269–307, https://doi.org/10.1179/imtr.1980.25.1.269.
[34] B. Gludovatz, S. Wurster, T. Weingartner, A. Hoffmann, R. Pippan, Influence of impurities on the fracture behaviour of tungsten, Philos. Mag. 91 (2011) 3006–3020, https://doi.org/10.1080/14786435.2011.558861.
[35] C. Ren, Z.Z. Fang, M. Koopman, B. Butler, J. Paramore, S. Middlemas, Methods for improving ductility of tungsten - a review, Int J. Refract Met. Hard Mater. 75 (2018) 170–183, https://doi.org/10.1016/j.ijrmhm.2018.04.012.
[36] M.G. Jo, P.P. Madakashira, J.Y. Suh, H.N. Han, Effect of oxygen and nitrogen on microstructure and mechanical properties of vanadium, Mater. Sci. Eng. A 675 (2016) 92–98, https://doi.org/10.1016/j.msea.2016.08.040.
[37] M.G. Ulitchny, R. Gibala, The effects of interstitial solute additions on the mechanical properties of niobium and tantalum single crystals, J. Less-Common Met. 33 (1973) 105–116, https://doi.org/10.1016/0022-5088(73)90061-1.
[38] "Standard Guide for Combustion, Inert Gas Fusion and Hot Extraction Instruments for use in Analyzing Metals, Ores, and Related," (2023) 1–10. ⟨https://doi.org/10.1520/E3346-22.1⟩.
[39] J.B. Nelson, D.P. Riley, An experimental investigation of extrapolation methods in the derivation of accurate unit-cell dimensions of crystals, Proc. Phys. Soc. 57 (1945) 160–177, https://doi.org/10.1088/0959-5309/57/3/302.
[40] D. Raabe, M. Herbig, S. Sandlöbes, Y. Li, D. Tytko, M. Kuzmina, D. Ponge, P. P. Choi, Grain boundary segregation engineering in metallic alloys: a pathway to the design of interfaces, Curr. Opin. Solid State Mater. Sci. 18 (2014) 253–261, https://doi.org/10.1016/j.cossms.2014.06.002.
[41] I. Langmuir, The adsorption of gases on plane surfaces of glass, mica and platinum, J. Am. Chem. Soc. 40 (1918) 1361–1403, https://doi.org/10.1021/ja02242a004.
[42] P. Lejcek, S. Hofmann, Thermodynamics of grain boundary segregation and applications to anisotropy, compensation effect and prediction, Crit. Rev. Solid State Mater. Sci. 33 (2008) 133–163, https://doi.org/10.1080/10408430801907649.
[43] John P. Perdew, K. Burke, M. Ernzerhof, Generalized gradient approximation made simple, Phys. Rev. Lett. 77 (1996), https://doi.org/10.1103/PhysRevLett.77.3865.
[44] P.E. Blöchl, Projector augmented-wave method, Phys. Rev. B 50 (1994) 17953–17979, https://doi.org/10.1103/PhysRevB.50.17953.
[45] G. Kresse, J. Furthmuller, Efficient iterative schemes for ab initio total-energy calculations using a plane-wave basis set, Phys. Rev. B 54 (1996), https://doi.org/10.1103/PhysRevB.54.11169.
[46] A. Van De Walle, P. Tiwary, M. De Jong, D.L. Olmsted, M. Asta, A. Dick, D. Shin, Y. Wang, L.Q. Chen, Z.K. Liu, Efficient stochastic generation of special

quasirandom structures, CALPHAD 42 (2013) 13–18, https://doi.org/10.1016/j.calphad.2013.06.006.
[47] D. Gehringer, M. Friák, D. Holec, Models of configurationally-complex alloys made simple, Comput. Phys. Commun. 286 (2023) 108664, https://doi.org/10.1016/j.cpc.2023.108664.
[48] H.J. Monkhorst, J.D. Pack, Special points for Brillouin-zone integrations, Phys. Rev. B 16 (1977) 1748–1749, https://doi.org/10.1103/PhysRevB.16.1748.
[49] Y.L. Hu, L.H. Bai, Y.G. Tong, D.Y. Deng, X.B. Liang, J. Zhang, Y.J. Li, Y.X. Chen, First-principle calculation investigation of NbMoTaW based refractory high entropy alloys, J. Alloy. Compd. 827 (2020), https://doi.org/10.1016/j.jallcom.2020.153963.
[50] D. Aksoy, M.J. McCarthy, I. Geiger, D. Apelian, H. Hahn, E.J. Lavernia, J. Luo, H. Xin, T.J. Rupert, Chemical order transitions within extended interfacial segregation zones in NbMoTaW, J. Appl. Phys. 132 (2022), https://doi.org/10.1063/5.0122502.
[51] I. Geiger, J. Luo, E.J. Lavernia, P. Cao, D. Apelian, T.J. Rupert, Influence of chemistry and structure on interfacial segregation in NbMoTaW with high-throughput atomistic simulations, J. Appl. Phys. 132 (2022), https://doi.org/10.1063/5.0130402.
[52] D. Aksoy, M.J. McCarthy, I. Geiger, D. Apelian, H. Hahn, E.J. Lavernia, J. Luo, H. Xin, T.J. Rupert, Chemical order transitions within extended interfacial segregation zones in NbMoTaW, J. Appl. Phys. 132 (2022), https://doi.org/10.1063/5.0122502.
[53] I. Geiger, J. Luo, E.J. Lavernia, P. Cao, D. Apelian, T.J. Rupert, Influence of chemistry and structure on interfacial segregation in NbMoTaW with high-throughput atomistic simulations, J. Appl. Phys. 132 (2022), https://doi.org/10.1063/5.0130402.
[54] S. Nose, A unified formulation of the constant temperature molecular dynamics methods, J. Chem. Phys. 81 (1984) 511–519, https://doi.org/10.1063/1.447334.
[55] P.M. Larsen, S.ø Schmidt, J. SchiØtz, Robust structural identification via polyhedral template matching, Model Simul. Mat. Sci. Eng. 24 (2016), https://doi.org/10.1088/0965-0393/24/5/055007.
[56] A. Stukowski, Visualization and analysis of atomistic simulation data with OVITO-the Open Visualization Tool, Model Simul. Mater. Sci. Eng. 18 (2010), https://doi.org/10.1088/0965-0393/18/1/015012.
[57] A. Jain, S.P. Ong, G. Hautier, W. Chen, W.D. Richards, S. Dacek, S. Cholia, D. Gunter, D. Skinner, G. Ceder, K.A. Persson, Commentary: the materials project: a materials genome approach to accelerating materials innovation, APL Mater. 1 (2013), https://doi.org/10.1063/1.4812323.
[58] N. Schoenberg, An x-ray investigation of the tantalum-oxygen system, Acta Chem. Scand. (1954).
[59] V.V. Klechkovskaya, V.I. Khitrova, An electron-diffraction study of the gamma phase in the ta-o system, Sov. Phys. Crystallogr 13 (1968) 428–430.
[60] O. Kubaschewski, B.E. Hopkins, Oxidation mechanisms of niobium, tantalum, molybdenum and tungsten, J. Less-Common Met. (1960) 172–180.
[61] G. Andersson, A. Magneli, Note on the crystal structure of niobium oxide, Acta Chem. Scand. (1957).
[62] K.K. Schulze, H.A. Jehn, G. Horez, High-temperature interactions of refractory metals with gases, J. Met. 40 (1988) 25–31.
[63] B. Ruscic, R.E. Pinzon, M.L. Morton, G. Von Laszevski, S.J. Bittner, S.G. Nijsure, K. A. Amin, M. Minkoff, A.F. Wagner, Introduction to active thermochemical tables: several 'Key' enthalpies of formation revisited, J. Phys. Chem. A 108 (2004) 9979–9997, https://doi.org/10.1021/jp047912y.
[64] J. Batey, Fractionation in gas inlets for PPA calibration, Vacuum 44 (1993) 639–642, https://doi.org/10.1016/0042-207X(93)90114-P.
[65] P.A. Redhead, Hydrogen in Vacuum Systems: An Overview, 254 (2003) 243–254. ⟨https://doi.org/10.1063/1.1597372⟩.
[66] M.L. Torti, Purification of tantalum obtained by vacuum arc melting, J. Electrochem Soc. 107 (1960) 33, https://doi.org/10.1149/1.2427604.
[67] M. Jovičević-Klug, I.R. Souza Filho, H. Springer, C. Adam, D. Raabe, Green steel from red mud through climate-neutral hydrogen plasma reduction, Nature 625 (2024) 703–709, https://doi.org/10.1038/s41586-023-06901-z.
[68] J.M. Oh, K.M. Roh, J.W. Lim, Brief review of removal effect of hydrogen-plasma arc melting on refining of pure titanium and titanium alloys, Int. J. Hydrogen Energy 41 (2016) 23033–23041, https://doi.org/10.1016/j.ijhydene.2016.09.082.
[69] L. Brinkman, B. Bulfin, A. Steinfeld, Thermochemical hydrogen storage via the reversible reduction and oxidation of metal oxides, Energy Fuels 35 (2021) 18756–18767, https://doi.org/10.1021/acs.energyfuels.1c02615.
[70] S.M. Howard, Ellingham Diagrams, MET 320 Metallurgical Thermodynamics. (n. d.).
[71] K. Naito, M. Tsuneo, Review on phase equilibria and defect structures in the niobium-oxygen system, Solid State Ion.-. 12 (1984) 125–134.
[72] J. Bygden, D. Sichen, S. Seetharaman, A thermodynamic study of the Molybdenum–Oxygen system, Metall. Mater. Trans. B 25B (1994), https://doi.org/10.1007/BF02662770.
[73] H.A. Wriedt, The O-W (oxygen-tungsten) system, Bull. Alloy Phase Diagr. 10 (1989) 368–384, https://doi.org/10.1007/BF02877593.
[74] S.P. Garg, N. Krishnamurthy, A. Awasthi, M. Venkatraman, Erratum to: the O-Ta (Oxygen-Tantalum) system, 407–407, J. Phase Equilibria 18 (1997), https://doi.org/10.1007/s11669-997-0076-9.
[75] L. Brewer, R.H. Lamoreaux, The Mo-O system (Molybdenum-Oxygen), Bull. Alloy Phase Diagr. 1 (1980) 85–89, https://doi.org/10.1007/BF02881199.
[76] L. Huang, L. Jiang, T.D. Topping, C. Dai, X. Wang, R. Carpenter, C. Haines, J. M. Schoenung, In situ oxide dispersion strengthened tungsten alloys with high compressive strength and high strain-to-failure, Acta Mater. 122 (2017) 19–31, https://doi.org/10.1016/j.actamat.2016.09.034.
[77] B.G. Butler, J.D. Paramore, J.P. Ligda, C. Ren, Z.Z. Fang, S.C. Middlemas, K. J. Hemker, Mechanisms of deformation and ductility in tungsten – a review, Int J. Refract Met. Hard Mater. 75 (2018) 248–261, https://doi.org/10.1016/j.ijrmhm.2018.04.021.
[78] M.W. Chase, NIST-JANAF thermochemical tables, Fourth Edition, J. Phys. Chem. Ref. Data Monogr. 9 (1998) 1–1951.
[79] A.H. Cottrell, Unified theory of effects of segregated interstitials on grain boundary cohesion, Mater. Sci. Technol. (U. Kingd.) 6 (1990) 806–810, https://doi.org/10.1179/mst.1990.6.9.806.
[80] W. Setyawan, R.J. Kurtz, Effects of transition metals on the grain boundary cohesion in tungsten, Scr. Mater. 66 (2012) 558–561, https://doi.org/10.1016/j.scriptamat.2012.01.002.
[81] K. Leitner, D. Scheiber, S. Jakob, S. Primig, H. Clemens, E. Povoden-Karadeniz, L. Romaner, How grain boundary chemistry controls the fracture mode of molybdenum, Mater. Des. 142 (2018) 36–43, https://doi.org/10.1016/j.matdes.2018.01.012.
[82] N.I. Medvedeva, Y.N. Gornostyrev, A.J. Freeman, Solid solution softening and hardening in the group-V and group-VI bcc transition metals alloys: first principles calculations and atomistic modeling, Phys. Rev. B Condens. Matter Mater. Phys. 76 (2007) 3–6, https://doi.org/10.1103/PhysRevB.76.212104.
[83] D.R. Trinkle, C. Woodward, The chemistry of deformation: how solutes soften pure metals, Science (1979) 310 (2005), https://doi.org/10.1126/science.311.5758.177.
[84] G. Liu, G.J. Zhang, F. Jiang, X.D. Ding, Y.J. Sun, J. Sun, E. Ma, Nanostructured high-strength molybdenum alloys with unprecedented tensile ductility, Nat. Mater. 12 (2013) 344–350, https://doi.org/10.1038/nmat3544.